

5-2015

## Surface Structure and Its Effect on Reducing Drag

Ragini Ramachandran

Follow this and additional works at: <https://commons.erau.edu/edt>



Part of the [Aerospace Engineering Commons](#)

---

### Scholarly Commons Citation

Ramachandran, Ragini, "Surface Structure and Its Effect on Reducing Drag" (2015). *Dissertations and Theses*. 277.

<https://commons.erau.edu/edt/277>

This Thesis - Open Access is brought to you for free and open access by Scholarly Commons. It has been accepted for inclusion in Dissertations and Theses by an authorized administrator of Scholarly Commons. For more information, please contact [commons@erau.edu](mailto:commons@erau.edu).

SURFACE STRUCTURE AND ITS EFFECT ON REDUCING DRAG

by

Ragini Ramachandran

A Thesis Submitted to the College of Engineering Department of Aerospace Engineering  
in Partial Fulfillment of the Requirements for the Degree of  
Master of Science in Aerospace Engineering

Embry-Riddle Aeronautical University  
Daytona Beach, Florida  
May 2015

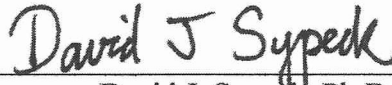
SURFACE STRUCTURE AND ITS EFFECT ON REDUCING DRAG

by

Ragini Ramachandran

This thesis was prepared under the direction of the candidate's Thesis Committee Chair, Dr. David J. Sypeck, Professor, Daytona Beach Campus, and Thesis Committee Members Dr. Eric Perrell, Professor, Daytona Beach Campus, and Dr. J. Gordon Leishman, Distinguished Professor, Daytona Beach Campus, and has been approved by the Thesis Committee. It was submitted to the Department of Aerospace Engineering in partial fulfillment of the requirements for the degree of Master of Science in Aerospace Engineering

Thesis Review Committee:



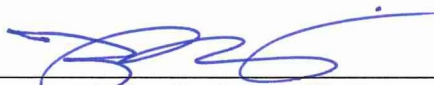
David J. Sypeck, Ph.D.  
Committee Chair



Eric Perrell, Ph.D.  
Committee Member



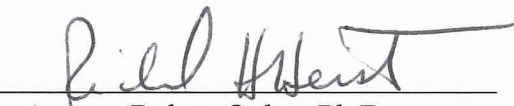
J. Gordon Leishman, Ph.D.  
Committee Member



Anastasios Lyrintzis, Ph.D.  
Chair, Aerospace Engineering  
or Yi Zhao, Ph.D.  
Graduate Program Coordinator



Maj Mirmirani, Ph.D.  
Dean, College of Engineering



for Robert Oxley, Ph.D.  
Associate Vice President, Academics

6/3/2015

Date

## Acknowledgements

I would like to express my gratitude towards my advisor, Dr. David J. Sypeck, for accepting this research as a thesis topic. He has constantly guided me and has been instrumental in designing and fabricating the miniature wind tunnel, which would not have been possible without him. He has spent many long hours carefully reviewing and purchasing the fabrication parts for the wind tunnel and test models, preparing the wing models with various fabrics, conducting the experiments, and also going through the thesis document. I would like to acknowledge prior support from the National Science Foundation (8802 Servohydraulic Test System), the ERAU College of Engineering (load cell), and the ERAU Department of Aerospace Engineering (small equipment and supplies). I thank the thesis committee members for accepting to be in the committee and also taking time to review my thesis. I express my gratitude to my parents for constantly urging me to perform better and for providing me with positivity, self-confidence, and will-power. I thank my friend, Peter Osterc, for supporting me during this research. Finally, I would like to express my sincere gratitude to God, with His grace and Divine Energy, this research has been possible.



## Abstract

Researcher: Ragini Ramachandran  
Title: Surface Structure and Its Effect on Reducing Drag  
Institution: Embry-Riddle Aeronautical University  
Degree: Master of Science in Aerospace Engineering  
Year: 2015

A miniature subsonic open return wind tunnel was designed and fabricated to measure drag on small test models at low Reynolds numbers. The wind tunnel featured a sensitive strain gauge type load cell. The average drag coefficient of sphere and cube test models were used to validate the miniature wind tunnel, and the values obtained were consistent with published results over the range of Reynolds numbers tested. These initial results gave confidence that the tunnel could be used to study the effects of surface finish on the drag of various models. Several fabrics with differing ribbed surface structures, including a Fastskin<sup>®</sup> FSI swimsuit fabric, were adhered to NACA 0012 wing models to assess their effectiveness in reducing drag at zero incidence. A similar wing model with an aircraft aluminum alloy skin with boundary layer trip strip served as a baseline for drag comparisons. The Fastskin<sup>®</sup> FSI swimsuit fabric and those with similar rib patterns tended to reduce drag below that of the baseline and the trend was maintained with increasing Reynolds number. Possible future research and drag reduction applications are also discussed.

## Table of Contents

	Page
Thesis Review Committee.....	ii
Acknowledgements.....	iii
Abstract.....	iv
List of Tables.....	vii
List of Figures.....	viii
List of Symbols.....	xi
Chapter	
1 Introduction.....	1
1.1 Boundary Layer Flows.....	2
1.2 Drag Reduction Techniques in Nature.....	4
1.3 Early Work on Riblets.....	9
1.4 Commercial Applications of Riblets.....	12
1.5 Experiments on Airfoils and Wing Models With Riblets.....	14
1.6 Present Research.....	17
2 Fundamental Experiments.....	18
2.1 Miniature Wind Tunnel.....	18
2.2 Drag Force Measurement.....	24
3 Ribbed Fabric Experiments.....	36
3.1 Preliminary Fabric Test.....	36
3.2 Final Fabric Test.....	45

4	Conclusions.....	62
4.1	Future Work.....	63
4.2	Potential Applications and Methods.....	63
	References.....	64
Appendices		
A	Bibliography.....	68
B	Additional Figures and Tables.....	69

## List of Tables

	Page
Table	
1.1 Experiments Performed on Airfoils with Riblets.....	16
2.1 Miniature Wind Tunnel Fabrication Components.....	23
2.2 Test Model Details.....	26
2.3 Average Drag Coefficient of Sphere.....	32
2.4 Average Drag Coefficient of Cube.....	32
3.1 Average Drag Coefficient of Preliminary Fabric Test.....	44
3.2 Average Drag Coefficient of Final Fabric Test.....	49
3.3 Average Drag Coefficient of Aluminum + Trip.....	53
B1 Test Model Details.....	71
B2 Product Information and Equipment Information.....	72
B3 Fabric Details.....	73

## List of Figures

	Page
Figure	
1.1	Laminar and Turbulent Boundary Layers.....2
1.2	Laminar to Turbulent Flow Transition over a Flat Plate.....3
1.3	Skin Friction and Pressure Drag.....3
1.4	Sailfish (left) and V-Shaped Protrusions (right).....5
1.5	Coronal Scale Pattern of Bat Hair.....6
1.6	Riblet Patterns on the Skin of Fast-Swimming Sharks.....7
1.7	SEM Image of Shark Denticles.....7
1.8	Flow Visualization on a Flat Plate (above); Riblet Surface (below).....8
1.9	Three-Dimensional View of Ridges.....9
1.10	Ridges Applied to the Upper Surface of a Laminar Flow Wing.....10
1.11	Riblets on the Surface of a Wing.....11
1.12	V-Shaped Riblets.....11
1.13	Typical Riblet Geometries.....12
1.14	3M Riblet Film on an Airfoil.....13
1.15	SEM Image of the Fastskin® FSI Swimsuit.....14
2.1	Honeycomb Specifications.....19
2.2	Load Cell.....20
2.3	Miniature Wind Tunnel.....22
2.4	Drawing of Pitot-Static Tube.....25
2.5	Test Models (a) Sphere and (b) Cube.....26

2.6	Velocity Profile of Test Section at 20 m s <sup>-1</sup> .....	27
2.7	Sting at 20 m s <sup>-1</sup> .....	29
2.8	Sting + Sphere at 20 m s <sup>-1</sup> .....	29
2.9	Sting + Cube at 20 m s <sup>-1</sup> .....	30
2.10	Drag Coefficients of Various Shapes.....	33
2.11	Average Drag Coefficient of Sphere and Cube Versus Reynolds number.....	34
2.12	Drag Coefficient of Smooth Sphere.....	34
3.1	NACA 0012 Wing Models with Fabrics. (a) Navy Blue; (b) Fastskin® FSI; (c) Purple; (d) Pattern; (e) Beige Thin; (f) Diamond; (g) Sky Blue; (h) Black; (i) Light Pink; (j) Corduroy; (k) Beige Thick; (l) Herringbone; (m) Gold; (n) Purple Stripe.....	38
3.2	Navy Blue.....	39
3.3	Fastskin® FSI.....	39
3.4	Purple.....	39
3.5	Pattern.....	40
3.6	Beige Thin.....	40
3.7	Diamond.....	40
3.8	Sky Blue.....	41
3.9	Black.....	41
3.10	Light Pink.....	41
3.11	Corduroy.....	42
3.12	Beige Thick.....	42
3.13	Herringbone.....	42
3.14	Gold.....	43
3.15	Purple Stripe.....	43

3.16	Final Wing Test Models. (a) 2024-T3 aluminum; (b) Fastskin <sup>®</sup> FSI; (c) Beige Thin; (d) Herringbone.....	46
3.17	Sting at 30 m s <sup>-1</sup> .....	47
3.18	Sting + Aluminum at 30 m s <sup>-1</sup> .....	47
3.19	Sting + Fastskin <sup>®</sup> FSI at 30 m s <sup>-1</sup> .....	48
3.20	Sting + Beige Thin at 30 m s <sup>-1</sup> .....	48
3.21	Sting + Herringbone at 30 m s <sup>-1</sup> .....	49
3.22a	Aluminum Wing Model with Boundary Layer Trip Strip (side view).....	51
3.22b	Aluminum Wing Model with Boundary Layer Trip Strip (front view).....	52
3.23	Sting + Aluminum + Trip at 30 m s <sup>-1</sup> .....	52
3.23a	Delta Average Drag Coefficient of Preliminary Fabric Test.....	54
3.23b	Delta Average Drag Coefficient of Preliminary Fabric Test.....	54
3.23c	Delta Average Drag Coefficient of Preliminary Fabric Test.....	55
3.23d	Delta Average Drag Coefficient of Preliminary Fabric Test.....	55
3.23e	Delta Average Drag Coefficient of Preliminary Fabric Test.....	56
3.24	Average Drag Coefficient of Aluminum Wing Model (with and without boundary layer trip strip) .....	57
3.25	Delta Average Drag Coefficient of Final Fabric Test.....	57
3.26	Laminar and Turbulent Boundary Layers on an Airfoil.....	58
B1	Test Models.....	69
B2	Wooden Bird with Chart Paper Background.....	69
B3	Test Models at 15 m s <sup>-1</sup> .....	70
B4	Average Drag Coefficient of Test Models.....	71

## List of Symbols

### Symbol

$\alpha$	Angle of Attack
$b$	Wingspan
$c$	Chord
$C_D$	Drag Coefficient
$\overline{C_D}$	Average Drag Coefficient
$\overline{C_{D \text{ Aluminum}}}$	Average Drag Coefficient of Aluminum
$\overline{C_{D \text{ Aluminum + Trip}}}$	Average Drag Coefficient of Aluminum + Trip Strip
$\overline{C_{D \text{ Cube}}}$	Average Drag Coefficient of Cube
$\overline{C_{D \text{ Fabric}}}$	Average Drag Coefficient of Fabric
$\overline{C_{D \text{ Sphere}}}$	Average Drag Coefficient of Sphere
$c_r$	Root Chord
$c_t$	Tip chord
$d$	Diameter
$D$	Drag Force
$\overline{D}$	Average Drag Force
$\Delta$	Delta or Difference
$h$	Riblet Height
$h^+$	Scaling Based on a Characteristic Height
$L$	Characteristic Length



$\mu$	Dynamic Viscosity
$n$	Height Above the Surface
$\nu$	Kinematic Viscosity
$Re$	Reynolds number
$\rho$	Density
$S$	Reference Area
$t$	Time
$T$	Period
$\tau_w$	Wall Shear Stress
$u$	Streamwise Velocity Component
$u'$	Fluctuating Component of Streamwise Velocity Vector
$\bar{u}$	Mean Streamwise Velocity
$v$	Wall-Normal Velocity Component
$V$	Flow Velocity of Air
$V_\infty$	Freestream Velocity
$w$	Spanwise Velocity Component
$x$	Streamwise Coordinate
$y$	Wall-Normal Coordinate
$z$	Spanwise Coordinate

## Chapter 1

### Introduction

The issue of drag is important for any body that moves through a fluid, including most classes of flight vehicles. A significant component of total drag is the shear stress or skin friction drag on the surface of the body, which is related to the velocity gradients in the flow in the boundary layer near the surface. For a laminar flow, the skin friction is obtained using Newton's formula, i.e.,

$$\tau_w = \mu \left( \frac{dV}{dn} \right) \Big|_{n \rightarrow 0} \quad (1)$$

where  $\tau_w$  is the shear stress exerted on the wall,  $\mu$  is the dynamic viscosity of a fluid, and  $dV/dn$  is the velocity gradient where  $V$  is the flow velocity and  $n$  is the height above the surface [1]. For a turbulent flow, there are additional turbulent terms that contribute to skin friction. Generally, to minimize drag on a body, it is more desirable to have larger regions of laminar flow. However, in practice laminar boundary layers are typically only obtained over short downstream distances and at most operating conditions bodies are covered with turbulent boundary layers. Therefore, to reduce net drag requires either encouraging the boundary layer to remain laminar to a greater downstream distance or to try to decrease the drag associated with the effects of the turbulent boundary layer. The work reported in this thesis examines the latter, and the effect of surface skin materials on skin friction drag.

## 1.1 Boundary Layer Flows

The flow of air along a surface often begins in laminar form, in which there is very little mixing between the layers of the fluid. Laminar flows exert low skin friction on surfaces. As the flow proceeds downstream, a laminar flow will generally transition to a turbulent flow, in which there is greater mixing between the fluid layers, steeper velocity gradients near the wall, and so higher skin friction drag. In this case, the drag force on a body will increase [2]. Figure 1.1 shows a diagram of laminar and turbulent boundary layers. Figure 1.2 shows a flow visualization of the laminar to turbulent transition on a flat plate. Figure 1.3 shows skin friction drag and pressure drag on blunt bodies and streamlined bodies. The drag on streamlined bodies is dominated by skin friction drag.

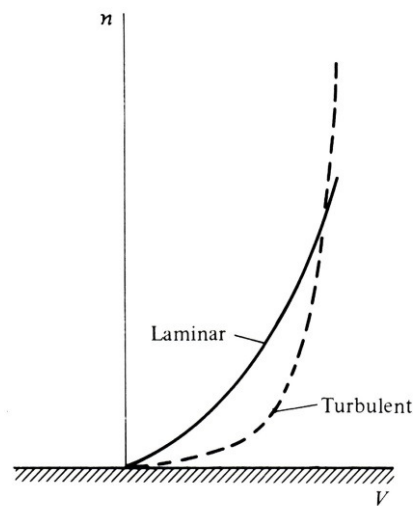


Figure 1.1. Laminar and Turbulent Boundary Layers [1].

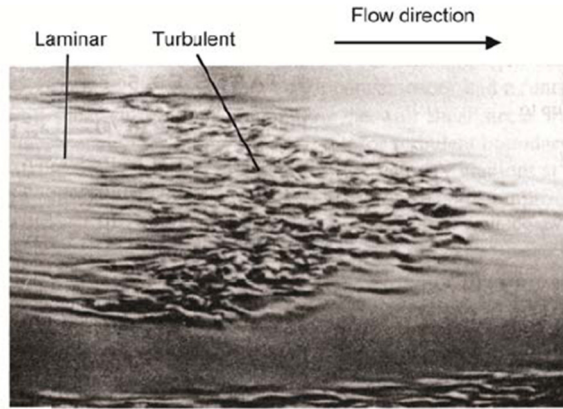


Figure 1.2. Laminar to Turbulent Flow Transition over a Flat Plate [3].

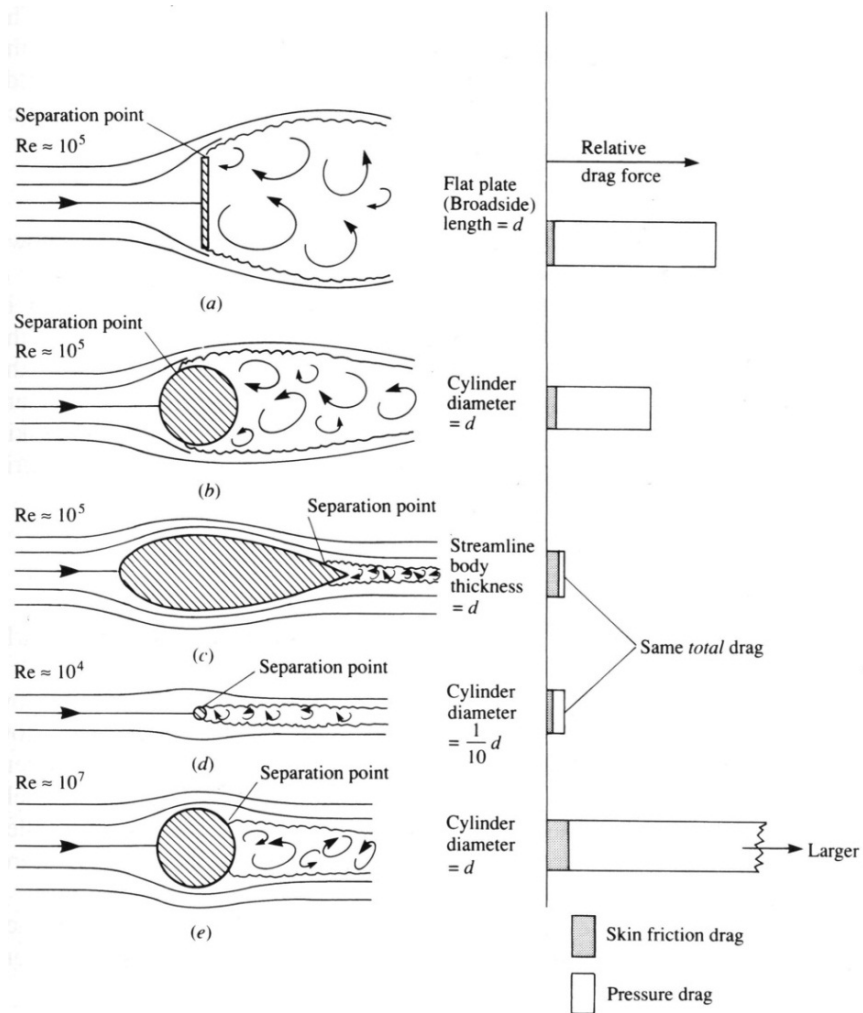


Figure 1.3. Skin Friction Drag and Pressure Drag [1].

The transition point to turbulent flow can be instigated by surface roughness, exterior disturbance sources, and adverse pressure gradients [2]. The first and second effects may be minimized by the fabrication of smooth surfaces and a non-turbulent free-stream flow environment. The effect of adverse pressure gradient is more difficult to overcome, in that pressure gradients are a function of the body shape and flight condition and can only be minimized by careful design [2]. Methods of drag reduction in the case of turbulent boundary layers also include mechanisms to remove the growing boundary layer, such as surface suction. Other mechanisms of drag reduction include so-called riblets. Traditional riblets are manufactured films or “skins” with small V-shaped grooves that are then applied over surfaces with their grooves aligned in the downstream direction. At the boundary layer level, riblets produce ordered modifications of the wall surface that affect the near-wall turbulent flow structures and are oriented in such a way that fluid mixing and the production of turbulence and the associated stresses is slowed [4]. The study of drag reduction using riblets has been an area of extensive research.

## **1.2 Drag Reduction Techniques in Nature**

Nature has also created ways of reducing drag in fluid flows. This has been observed by the efficient movement of fish such as sailfish, marlins, and sharks, as well as bats, birds, insects and so on [5]. The V-shaped protrusions on the skin of a sailfish were investigated by Sagong et al. using Direct Numerical Simulation (DNS) [6]. Sailfish are the fastest marine animals that can reach speeds of  $110 \text{ km h}^{-1}$  [6]. Sagong et al. estimated a 5% reduction in skin friction drag from the skin but concluded that the

pressure drag on these protrusions lead to an increase in total drag [6]. Figure 1.4 shows a sailfish and the protrusions on its skin.

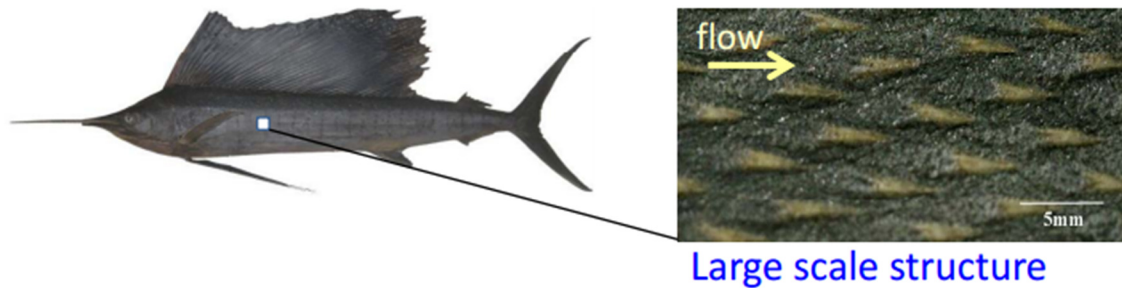


Figure 1.4. Sailfish (left) and V-Shaped Protrusions (right) [6].

Bullen and McKenzie [7] measured aspects of the head and body pelage of 23 species of Western Australian bats. They found a functionally appropriate relationship between the normal flight speeds and foraging strategy of the bats at three levels of geometric consideration: the overall fur texture, individual hair length, and cuticular scale attributes (outer layer of the hair). It was concluded that the species that utilize high-speed and aerodynamically efficient flight had fur within the non-dimensional height range of  $8 < h^+ < 15$ , where  $h^+ = hu/\nu$  is the scaling based on a characteristic height (height of the fur of bats in this case) [7],  $h$  is the fur (or riblet) height,  $u$  is the flow velocity, and  $\nu$  is the kinematic viscosity. Figure 1.5 shows the coronal scale pattern of bat hair, which is actually similar to manufactured riblets.

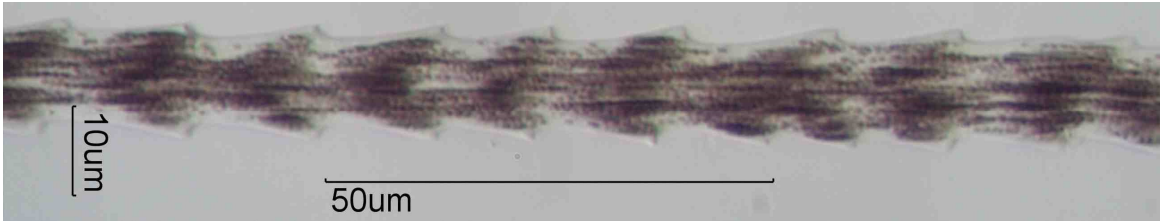


Figure 1.5. Coronal Scale Pattern of Bat Hair [8].

The skin of fast swimming sharks reduces drag and also protects the shark against biofouling (accumulation of microorganisms, plants, algae, or animals on wetted surfaces) as they swim through water [5]. The tiny scales covering the skin of sharks, known as dermal denticles (i.e., scales), are often shaped like small riblets and aligned in the direction of fluid flow [5]. The cross-sectional shape of the shark skin riblets greatly varies, even at different locations on the same shark [5]. Figure 1.6 shows the riblet patterns on the skin of several different fast-swimming sharks. Figure 1.7 shows a SEM (Scanning Electron Microscope) image of shark denticles.

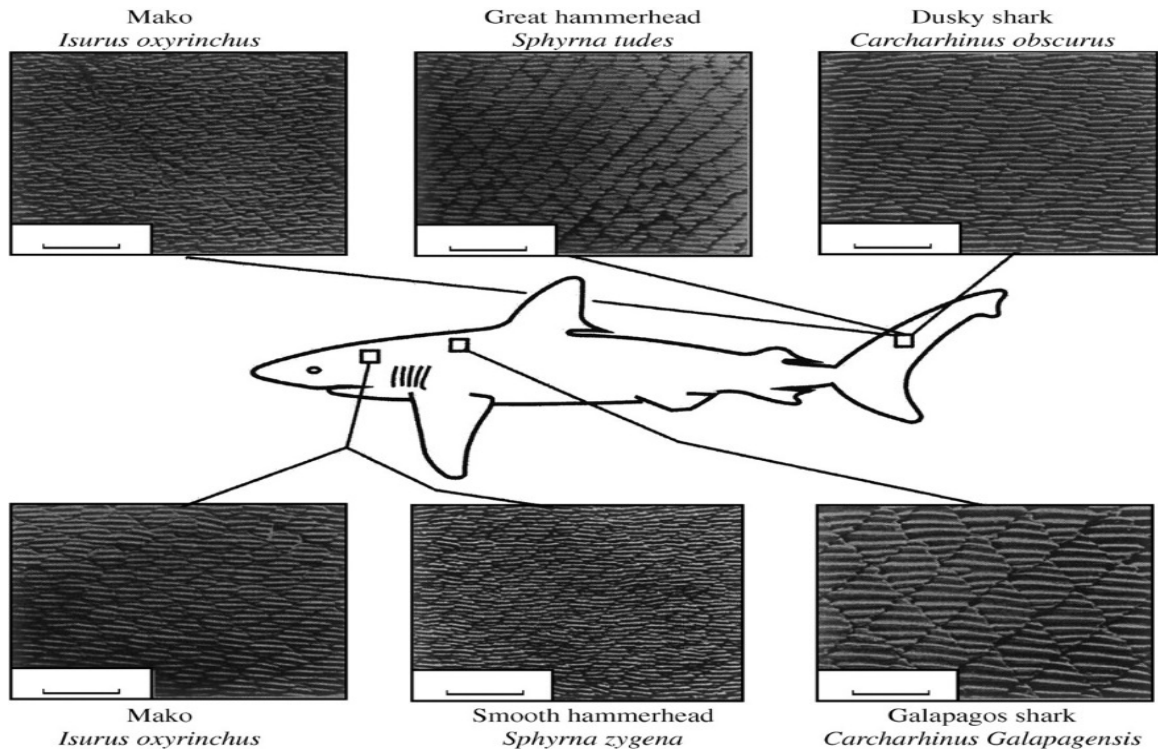


Figure 1.6. Riblet Patterns on the Skin of Fast-Swimming Sharks [5].  
Size scale bar is 0.5 mm.

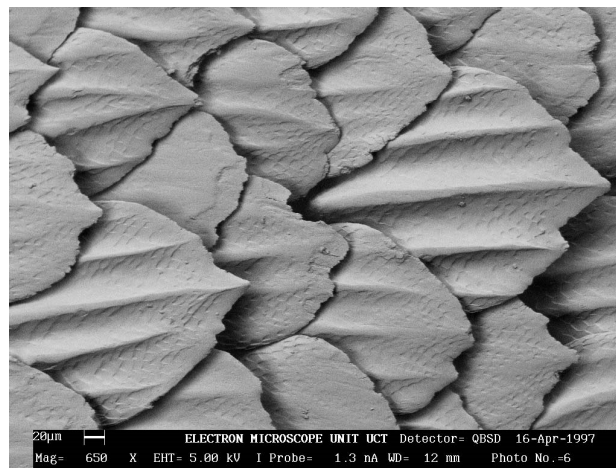


Fig. 1.7. SEM Image of Shark Denticles [9].  
Size scale bar is 20 µm.



The small denticles or riblets on the surface of these sharks are believed to reduce the increased drag associated with turbulent flows in two ways: 1) Impeding the cross-stream translation of the streamwise eddies in the sublayer and 2) Elevating the stronger eddies further above the surface, thereby reducing the shear stress and momentum transfer [5]. The first mechanism, in which the riblets interact with and impede the translation of eddies is complex, and the behavior is not yet fully understood. On a practical level, impeding the movement of eddies reduces the occurrence of ejections into the outer parts of the boundary layers, thereby decreasing momentum transfer caused by the tangling and twisting of eddies in the outer boundary layers [5]. Figure 1.8 shows the flow visualization performed on a flat plate and on a riblet surface.

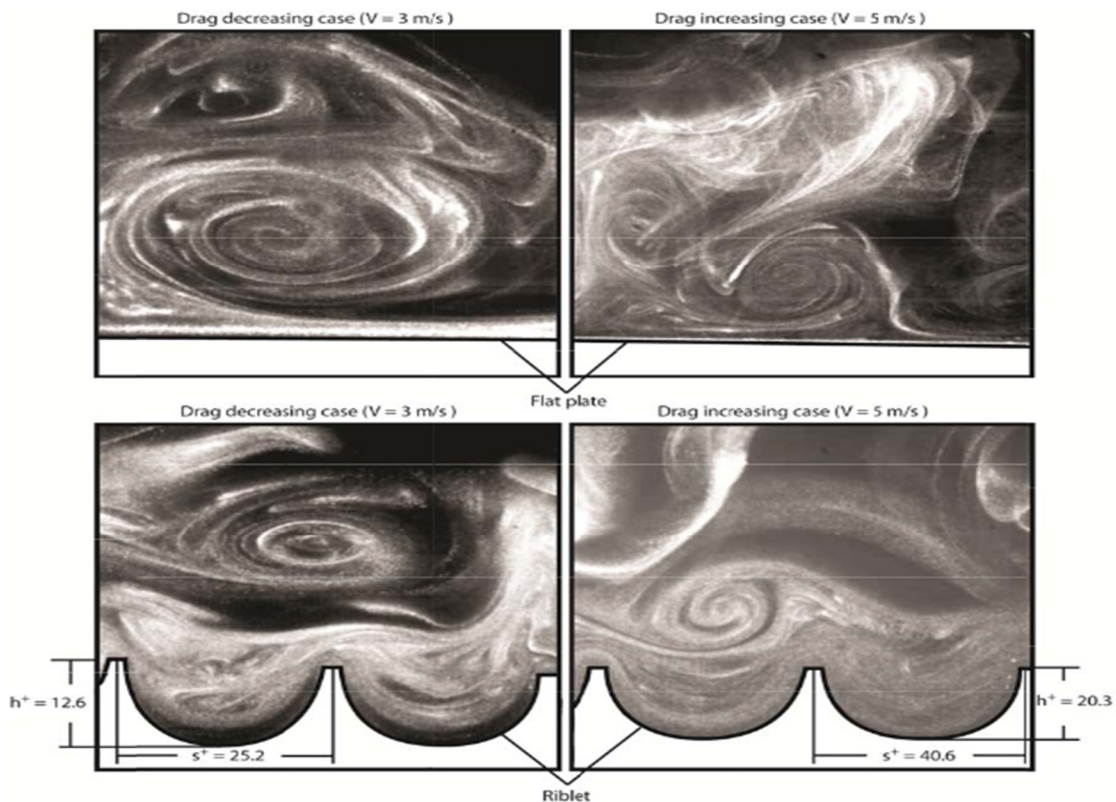


Figure 1.8. Flow Visualization on a Flat Plate (above); Riblet Surface (below) [5].

### 1.3 Early Work on Riblets

An early attempt to reduce drag using riblets and also delay turbulent flow transition was reported by Rethorst in 1969 [2]. His invention comprised of a series of ridges or waves integrated with a solid surface oriented at some angle to or parallel to the free stream velocity vector. These ridges were thought to energize the boundary layer by providing paths for utilization of cross flow components and for acceleration of the flow relative to the normal surface of the body [2], sometimes called the channeling effect. Figure 1.9 and Figure 1.10 show the applications of these ridges on wing sections.

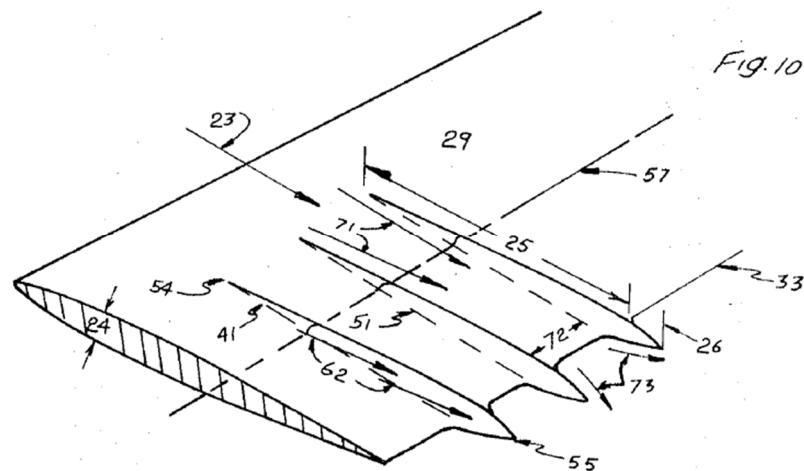


Figure 1.9. Three-Dimensional View of Ridges [2].

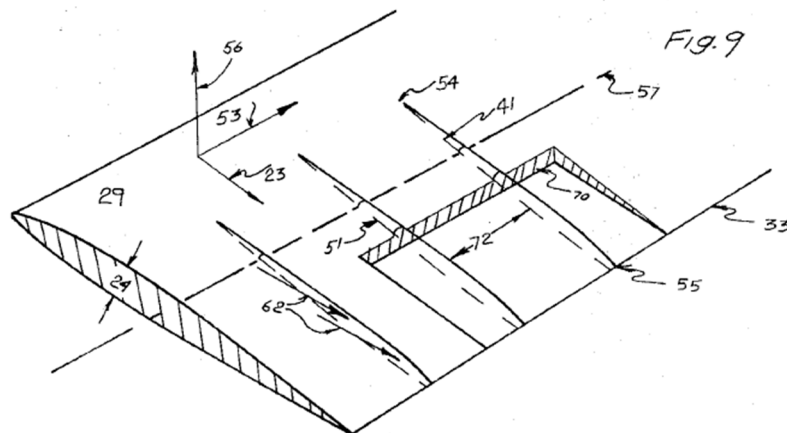


Figure 1.10. Ridges Applied to the Upper Surface of a Laminar Flow Wing [2].

In 1984, Walsh was credited with a system of flow control devices that resulted in reduced skin friction on aerodynamic and hydrodynamic surfaces [10]. The development was achieved by modifying the surface by micro-geometries [10]. His experimental data indicated that the turbulent boundary layer consists of at least three disparate type scales of motion. One of these involve large eddies with scales on the order of the boundary layer thickness exist in the outer region and comprise the vortical or non-vortical interface of the boundary layer with the inviscid freestream flow [10]. Figure 1.11 shows the riblet geometry and its location on the surface of a wing. Figure 1.12 shows the V-shaped riblets.

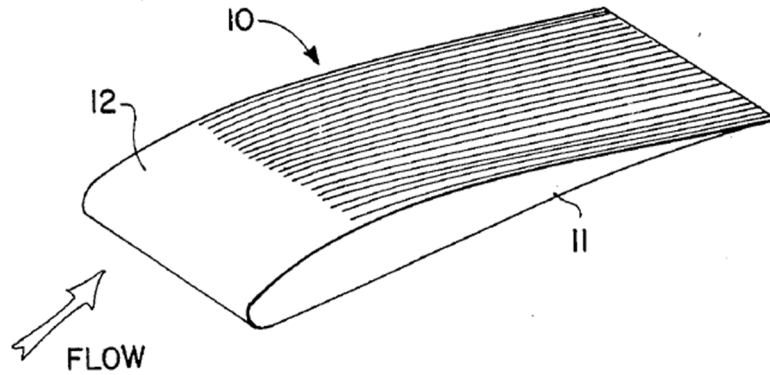


Figure 1.11. Riblets on the Surface of a Wing [10].

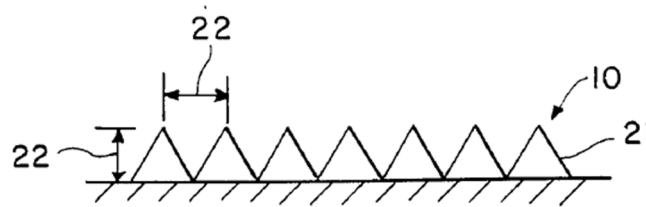


Figure 1.12. V-Shaped Riblets [10].  
*Riblet dimensions lie between 0.1 mm and 0.5 mm.*

More recent riblets can also be U-shaped, as shown in Figure 1.13 [4]. Experiments conducted by Walsh and Weinstein [11] and Liu et al. [12] reported reductions in burst frequency (frequency of breakup of vertical eddies). Bechert et al. [13], Choi [14] and others, have reported small amounts of total drag reduction up to 4% and skin friction drag reduction up to 10% by varying the geometry and the orientation of the riblets with respect to the airflow [15]. It should be noted that skin friction drag is only a fraction of the total drag. Because total drag is the sum of skin friction drag and pressure drag,

reductions of drag may only be possible under certain conditions such as at low angles of attack.

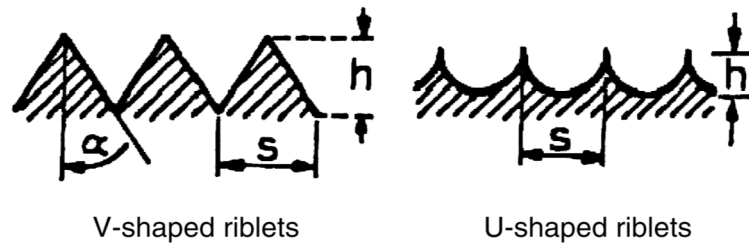


Figure 1.13. Typical Riblet Geometries [4].

#### 1.4 Commercial Applications of Riblets

Riblets with symmetric V-grooves (height equal to spacing) with adhesive backed film manufactured by the 3M Company have been widely investigated and the results have shown good consistency with regard to the degree of drag reduction as well as certain aspects of the flow structure [15]. Maximum skin friction drag reduction in the range of 4–8 % has been measured on a variety of two-dimensional flows with zero or mild pressure gradients [15]. Studies using 3M riblets have shown that the most favorable drag reduction occurs in the  $h^+$  range of 8–15. Some of the earlier studies at low speeds have focused attention on optimizing riblet geometry and skin friction drag reduction as high as 10% have been reported [15]. Figure 1.14 shows an airfoil with the 3M riblet film.

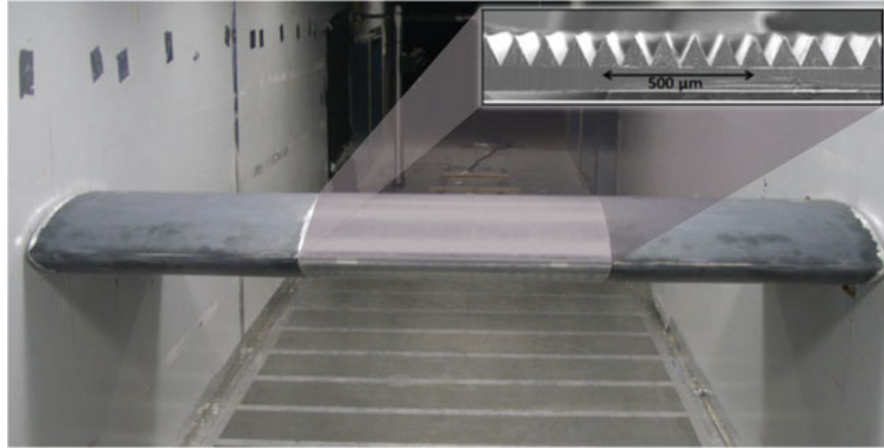


Figure 1.14. 3M Riblet Film on an Airfoil [16].

Inspired by the surface pattern on fast-swimming sharks, Speedo International Ltd. developed and then manufactured swimsuits to reduce skin friction drag on the body of swimmers [17]. The Fastskin<sup>®</sup> FSI utilizes a form of riblets on their swimsuits. Speedo<sup>®</sup> examined the texture of shark skins and their movement through water [18]. They found that there are more denticles covering some parts of the shark's body and in some places they are much longer or shorter (see Fig. 1.6). These denticles are slanted towards its tail, directing the flow of water around the shark's body, thereby reducing form or pressure drag [18]. Because of this, the shark can cruise the water silently. Speedo<sup>®</sup> recreated the function of these denticles by replicating the V-shaped ridges on the surface of the suit [18]. The Fastskin<sup>®</sup> FSI fabric consists of lycra/polyester fabric that has V-shaped ridges and a denticle surface print [18]. Figure 1.15 shows a SEM image of the Fastskin<sup>®</sup> FSI fabric.

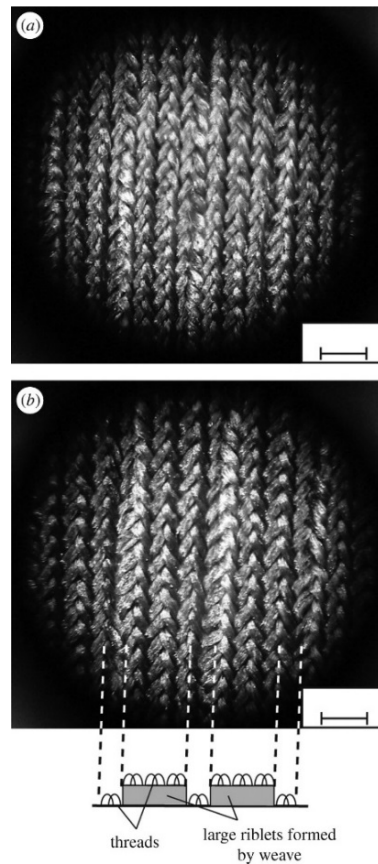


Fig. 1.15. SEM Image of the Fastskin<sup>®</sup> FSI Swimsuit [5].  
Scale bar is 1.0 mm.

### 1.5 Experiments on Airfoils and Wing Models With Riblets

Despite research during the last decades, the detailed mechanisms by which riblets reduce the wall shear stress are not clearly understood, even in a zero-pressure gradient boundary layer flow [15]. In recent years, measurements of both mean velocity and some turbulence statistics in the grooves have become available using machine cut riblets (of much larger size dimensions than the 3M riblets). These results indicate the wall shear stress is increased near the groove peaks and appreciably reduced in the valley so that net drag reduction results despite the increased wetted area of the grooves [15].

More practical applications tend to involve situations with both pressure gradients and three-dimensionality. The boundary layer on an airfoil is subjected to the combined influence of streamwise pressure gradients and surface curvature. Measurements on airfoils at zero incidence have generally revealed drag reduction comparable to those on zero-pressure gradient flows; however, in very few of the investigations, the effect of airfoil incidence has been addressed [15].

Coustols and Cousteix [19] assessed the drag reduction on a LC100D airfoil at low speed when using 3M riblets. With riblets covering only the airfoil upper surface (or suction surface), drag measurements were made using a wake survey over an incidence range of  $0\text{--}6^\circ$ . They reported total drag reduction of about 2% at  $\alpha = 0^\circ$  and  $2^\circ$ , where  $\alpha$  is angle of attack, and no drag reductions were observed at higher values of  $\alpha$  [19]. The corresponding skin friction drag reduction was observed to be 7% [19]. The poor performance of riblets at higher  $\alpha$  was attributed partly to possible effects of boundary layer thickening and flow separation [19].

The effectiveness of 3M riblets on a CAST 7 supercritical airfoil at transonic speeds was reported by Coustols and Schmitt [20]. These authors showed total drag reduction of about 3.5% and a skin friction drag reduction of about 7–8% at  $h^+$  in the range of 12–16 [20]. For realistic configurations, solving the flow details at the riblet level is beyond the capabilities of present computers [4]. Therefore, a riblet submodel is needed to account for riblets in practical computations [3]. Table 1.1 summarizes several different experiments performed on airfoils with riblets and their measurement methods [15].



Table 1.1. Experiments Performed on Airfoils with Riblets [15].

Author	Airfoil	Chord, m	$Re_c$	$M_\infty$	h, mm	$\alpha^\circ$	$\Lambda^\circ$	Remarks
Airfoil Coustols	LC 100D	0.40	$5.3 - 7.95 \times 10^5$	-	0.152, 0.076	0 to 6		Skin friction drag reduction inferred from measured total drag reduction (wake survey)
Caram & Ahmed	NACA 0012	0.15	$2.5 \times 10^5$	-	0.152, 0.076, 0.023	0		Total drag reduction measured (wake survey)
Coustols & Smith	CAST 7	0.20	$3.3 \times 10^6$ (at $M_\infty = 0.76$ )	0.65 - 0.76	0.017, 0.023, 0.033, 0.051	0		Skin friction drag reduction inferred from measured total drag reduction (wake survey)
Viswanath & Mukund	ADA-S1	0.15	$3.0 \times 10^6$	0.60 - 0.76	0.018, 0.033	- 0.5 to 1.0		Skin friction drag reduction inferred from measured total drag reduction (wake survey)
Sundaram et al	NACA 0012	0.60	$1 \times 10^5$	-	0.152, 0.076	0 to 6		Skin friction drag reduction estimated from measured total drag reduction (wake survey)
Subashchander et al	NACA 0012	0.60	$1 \times 10^5$	-	0.152	6 to 12		Skin friction drag reduction estimated from measured total drag reduction (wake survey)
Subashchander et al	GAW-2	0.60	$1 \times 10^5$	-	0.076	0 to 12		Total drag reduction measured (wake survey)
Channaraju & Viswanath	GAW-2	0.60	$1 \times 10^5$	-	0.152, 0.076	0 to 6		Skin friction drag reduction inferred from measured total drag reduction (wake survey); base drag reduction also measured
SWEPT WING Coustols	ONERA D	0.20	$2.65 - 4.25 \times 10^5$	-	0.152, 0.076, 0.051	0	22.5	Skin friction drag reduction inferred from measured total drag reduction (wake survey)
Sundaram et al	GAW-2	0.45	$0.75 \times 10^6$	-	0.114	0 to 6	25	Skin friction drag reduction estimated from measured total drag reduction (wake survey)
WING-BODY Coustols & Smith	AIRBUS 320	mac:0.381	$3.9 \times 10^6$ (at $M_\infty = 0.70$ )	0.30 - 0.82	0.023	- 2 to 3	28	Total drag reduction measured (Balance)
Van Der Hoven & Bechert	Do228	0.508 (Centre section)	$1.37-3.09 \times 10^6$	-	0.076	- 5 to 20		Total drag reduction measured (Balance)

The velocity distribution around a solid cylinder covered with various fabrics (knitted, tweed, flannel, and denim) was studied experimentally in a wind tunnel by T. Watanabe, T. Kato, and Y. Kamata using hot-wire anemometry [21]. They explained that flow field can be divided into three regions: 1) The outer field of the fabric layer; 2) The field in the fabric; 3) The field between the inner surface of the fabric and the surface [21]. They concluded that the velocity in the inner flow field increases proportionally to the permeability of the fabric and by piling the fabrics, the penetration of airflow could be minimized [21].

## **1.6 Present Research**

In the present research, surface finishes or skins have been studied in an effort to reduce the drag force on small models. First, a small wind tunnel was designed and fabricated featuring a high fidelity strain gauge load cell to measure the drag force acting on the test models. Next, NACA 0012 wing models were covered with various skins or fabrics and tested at zero incidence in the wind tunnel. A smooth and rough wing model was used as a baseline for comparison of drag force with the fabric test models, the objective being to determine the effects of the fabrics on the boundary layer skin friction drag. The overall objective of the study was to determine if there was any drag reduction benefits that could be produced by the addition of the fabrics, at least over the operational conditions allowed by the constraints of the wind tunnel.

## Chapter 2

### Fundamental Experiments

This chapter describes the experiments that were conducted, including the design of the miniature wind tunnel, the balance, and the data acquisition system. This chapter concludes with a description of measurements made for standard test articles to validate the experimental setup.

#### 2.1 Miniature Wind Tunnel

A miniature, open-return subsonic wind tunnel was designed, fabricated and used for the purpose of measuring the effectiveness of the drag reduction on bodies and wing models covered with different fabrics or “skins”. A sensitive strain gauge type load cell was used to measure the drag on the bodies. The components of the wind tunnel are discussed in this section.

The entrance or intake was made of PVC (polyvinyl chloride) DWV pipe having dimensions of 7.6 cm (3 in) x 15.2 cm (6 in) [22]. The settling chamber present in the intake consisted of one honeycomb and two plain square woven screens on either side. The first screen, which was placed before the honeycomb, was a 10 x 10 mesh corrosion-resistant type 304 stainless steel wire cloth with an opening size of 0.196 cm (0.077 in), open area of 59%, and wire diameter of 0.058 cm (0.023 in) [23]. An aluminum honeycomb having a hexagonal core was used as a flow straightener and turbulence reducer in the wind tunnel. The length and cell hydraulic diameter are key factors in the selection of honeycombs [24]. The type used had an average cell size of 0.64 cm (0.25 in)

and length of 7.62 cm (3 in). Figure 2.1 shows typical specifications of hexagonal honeycombs. The second screen, present immediately after the honeycomb, was a 15 x 15 mesh corrosion-resistant type 304 stainless steel wire cloth having an opening size of 0.145 cm (0.057 in), open area of 73%, and wire diameter of 0.025 cm (0.01 in) [25].

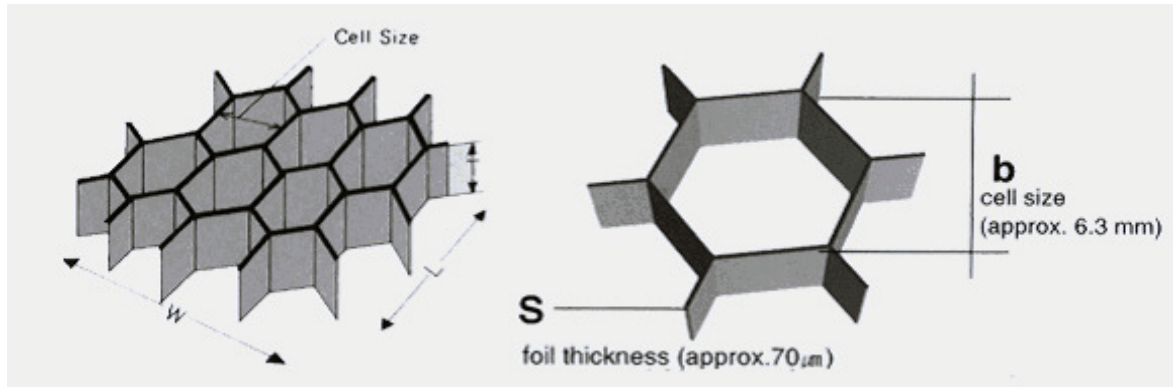


Figure 2.1. Honeycomb Specifications [26].

The test section was made of an impact-resistant polycarbonate round tube with an OD (Outer Diameter) of 8.9 cm (3.50 in), an ID (Inner Diameter) of 7.6 cm (3 in), with corresponding wall thickness of 0.64 cm (0.25 in), and a length of 61.0 cm (24 in) [42]. The polycarbonate tube is also resistant to wear and maintains good clarity [27].

The end assembly was a PVC pipe having dimensions of 5.1 cm (2 in) x 7.6 cm (3 in) [22]. Another PVC pipe having a length of 5.1 cm (2 in) was present after the end assembly containing a hole for the sting and mounting holes for the load cell. The terminology “end assembly” is used rather than “diffuser” because the diameter is actually smaller than the test section. A valve was used to control the flow rate in the wind tunnel to obtain different flow velocities. The body and ball were PVC and the seal was EPDM (ethylene propylene diene monomer, M-class) [28].

The fan used for operating the tunnel was the type LL600 [29]. A vacuum hose was used to connect the vacuum to the end assembly of the wind tunnel. This fan on its own was able to generate a maximum velocity of about  $18 \text{ m s}^{-1}$ . Velocities up to about  $35 \text{ m s}^{-1}$  were achieved by connecting two more similar fans in parallel.

The force measurement device was an Instron 2530-439 high fidelity strain gauge load cell with maximum capacity of  $\pm 5 \text{ N}$  was used for measuring drag force. Instron load cells are precision force transducers consisting of strain gauges bonded to the internal load bearing structures [30]. When the load cell is stressed mechanically, the electrical resistance of the strain gauge varies which in turn changes the output signal. The load cell structure has high axial stiffness, which reduces the stored energy that could otherwise transfer to the specimen thereby giving errors [30]. Increased lateral stiffness reduces measurement errors from off axis loading that are found when performing compression and flexural tests. These load cells are designed for both tension and compression. Figure 2.2 shows a photograph of the load cell.

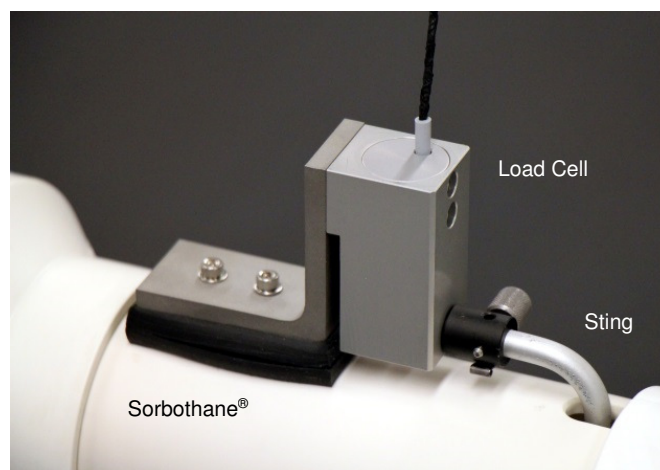


Figure 2.2. Load Cell.

The drag force was recorded using a FastTrack 8800 data acquisition system. The measured force was displayed in gf (gram-force), where  $1 \text{ gf} = 0.00981 \text{ N}$ . The data were captured at a rate of  $0.1 \text{ kS s}^{-1}$  and plotted in real time using Instron DAX V9.1 software. The load cell was mounted outside the wind tunnel to avoid interference from the airflow. To dampen vibrations from the walls of the wind tunnel, the load cell mount was placed on two layers of Sorbothane<sup>®</sup> [31]. Both layers had a thickness of 0.64 cm (0.25 in). Sorbothane<sup>®</sup> is known for attenuating shock, isolating vibrations, and damping noise [32]. The average accuracy of the load cell was about 0.01 g (by running average) over the range of interest was verified by orienting the sting vertically, and then weighing 1, 2, 5, 10 and 20 g Class S-1 and 100 g Class F precision calibration weights.

The sting for mounting the test articles (models) was a solid anodized aluminum rod. It was a 6063-T5 type aluminum rod with an OD of 0.64 cm (0.25 in) and had a length of approximately 38.1 cm (15 in) [33]. The sting was carefully bent (no heat treatment was necessary) and inserted into the load cell. The forces generated on the models were transmitted to the load cell through the sting.

A pitot-static probe with manometer measured upstream differential pressure. Manometer accuracy to 0.001 kPa was verified using a shared pressure source and a pressure calibrator. Figure 2.3 shows a photograph of the miniature wind tunnel and Table 2.1 gives a list of the fabrication components.

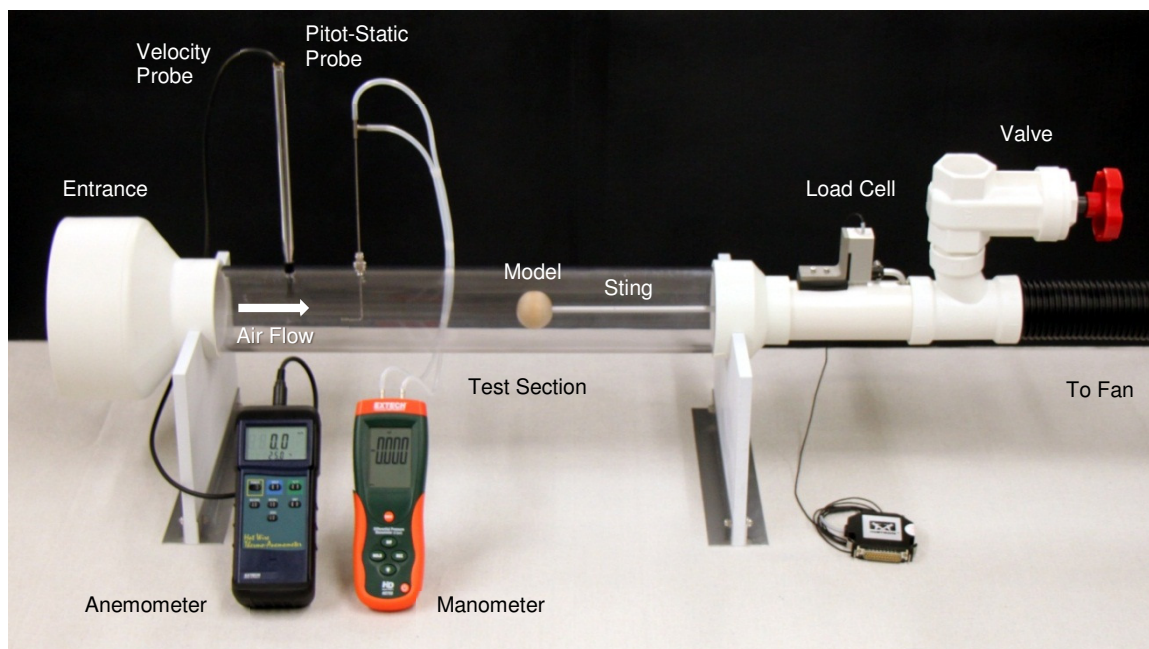


Figure 2.3. Miniature Wind Tunnel.

Table 2.1. Miniature Wind Tunnel Fabrication Components.

Component	Specification	Manufacturer/Supplier
Entrance	Sch 40 PVC, 3 x 6 in Pipe Increaser-Reducer	Charlotte Pipe and Foundry (Charlotte, NC)
Honeycomb	Al alloy, 3 in thick, ¼ in cell, 0.0025 in wall	-
Screens	304 stainless steel, 10 x 10 mesh (0.023 in wire) and 15 x 15 mesh (0.010 in wire)	McMaster-Carr Supply Co. (Elmhurst, IL)
Test Section	Impact resistant polycarbonate, 3 ½ x 3 x 24 in	McMaster-Carr Supply Co. (Elmhurst, IL)
End Assembly	Sch 40 PVC, 2 x 3 in Pipe Increaser-Reducer, 2 in Pipe, 2 x 1 ½ x 2 in Reducing Tee, 1 ½ in Pipe	Charlotte Pipe and Foundry (Charlotte, NC)
Valve	PVC Gate Valve, 1 ½ in socket weld	King Bros. Industries (Valencia, CA)
Fan	Model LL600, 6.0 peak HP	Shop-Vac Corp. (Williamsport, PA)
Sting	Anodized 6063-T5, ¼ in DIA	The Hillman Group (Cincinnati, OH)
Load Cell	2530-439, ±5 N capacity, high fidelity strain gauge	Instron (Norwood, MA)
Mount	304 stainless, 3/16 x 2 ½ in	McMaster-Carr Supply Co. (Elmhurst, IL)
Vibration Damper	Sorbothane®, ¼ in thick, 70 OO durometer	Sorbothane, Inc. (Kent, OH)
Velocity Probe	407123 Heavy Duty Hot Wire Thermo-Anemometer, 20+ m/s and 50°C capacity, 0.1 m/s and 0.1°C resolution, digital	Extech Instruments (Nashua, NH)
Pitot-Static Probe	PAA-8-KL, 1/16 in stem diameter, Teflon® ferrule, 1/8 NPT connector	United Sensor Corp. (Amherst, NH)
Tubing	White silicone, 3/16 in OD, 1/32 in wall	Small Parts Inc., operated by Amazon.com (Seattle, WA)
Manometer	HD 755 Differential Pressure Manometer (0.5 psi), ±3.447 kPa capacity, 0.001 kPa resolution, digital	Extech Instruments (Nashua, NH)
Stand	PVC sheet, ½ in thick	Small Parts Inc., operated by Amazon.com (Seattle, WA)
Feet	Al alloy, 1/16 x 1 in	The Hillman Group (Cincinnati, OH)
Bolts, Locknuts, and Washers	18-8 stainless, M3-0.5 (load cell/mount), 10-32 (stand/feet)	McMaster-Carr Supply Co. (Elmhurst, IL)



## 2.2 Drag Force Measurement

To verify the performance of the wind tunnel, drag forces of fundamental shapes were measured. The models were a sphere and a cube. The tests were conducted as follows:

1. The models were first carefully mounted to the sting and placed inside the test section.
2. Next, the end assembly and the valve were tightly slid on to the other end of the test section.
3. The test models were checked for proper alignment with respect to the center line of the test section. The pitch and yaw angle of the models was also corrected if not zero.
4. The hot-wire anemometer probe was inserted into the anemometer hole, which was 7.5 cm from one end of the test section.
5. The pitot-static probe, which was 7.5 cm from the center of the anemometer hole, was lowered and connected to the manometer. Figure 2.4 shows the drawing of the pitot-static probe.
6. The fan was switched on and the velocity of the airflow was checked using both probes. Bernoulli's equation was used to confirm the differential pressure readings.
7. After this, the fan was turned off momentarily and both probes were raised to avoid affecting the flow on the test models.
8. The data acquisition software was started, the fan was turned on, and data was collected.

9. Details of a typical test involved starting the data acquisition, waiting for 15 s, turning the fan on for 60 s, turning off the fan, waiting for another 15 s, and stopping the data acquisition.

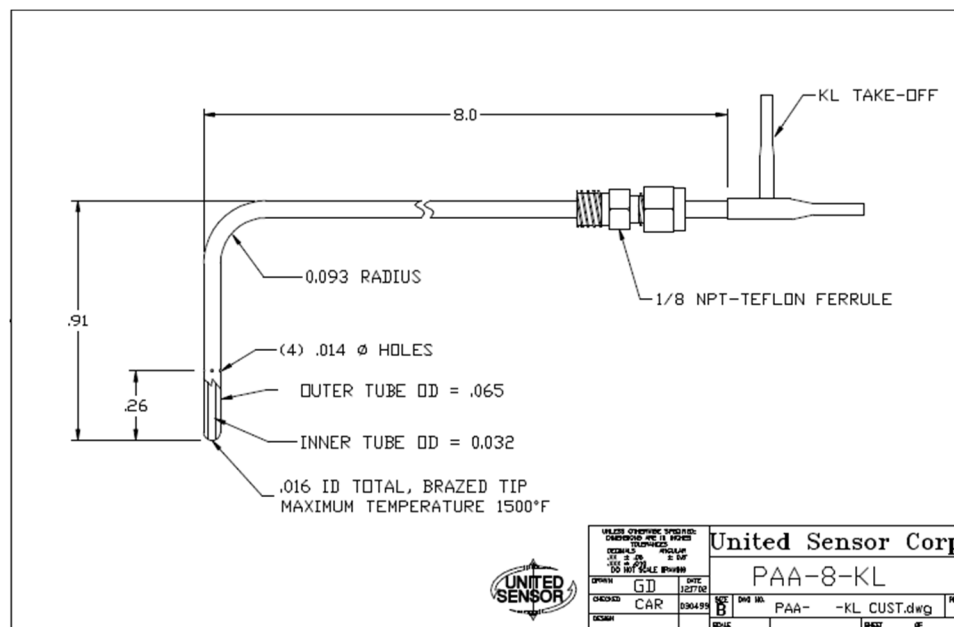


Figure 2.4 Drawing of Pitot-Static Probe [34].

A sphere and cube was chosen for performance verification testing. Figure 2.5 shows a photograph of the test models. The cube was sanded using a 320 grit SiC sandpaper to unify and smoothen the sides. A 6.35 mm (0.25 in) hole was drilled into each test model as needed for mounting onto the sting. The mounting holes for the sphere and cube were centrally located. Test model dimensions were measured using a Pittsburgh<sup>®</sup> 6 in Digital Caliper. Further test model details are listed in Table 2.2 where  $S$  is the reference area.

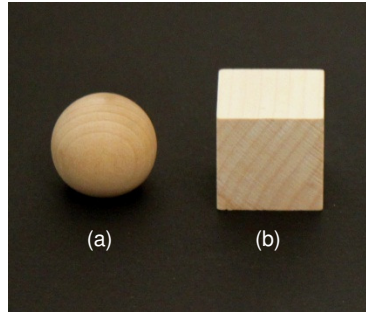


Figure 2.5. Test Models (a) Sphere and (b) Cube.  
The models are 2.54 cm (1 in).

Table 2.2. Test Model Details.

Test Model	Specification	Manufacturer/Supplier	Measured Dimension(s) (cm)	$S$ (cm <sup>2</sup> )
Sphere	Wood, Round Ball Knob, 1 in	The Hillman Group (Cincinnati, OH)	2.54 (diameter)	5.07
Cube	Wood, Square Cube, 1 in	The Hillman Group (Cincinnati, OH)	2.57 (side)	6.60

On the day of the initial tests, the reported atmospheric pressure was 102.133 kPa. The lab temperature was 295.7 K measured using a type K thermocouple. The ideal gas law was used to calculate ambient air density as  $\rho = 1.20 \text{ kg m}^{-3}$ . All testing days exhibited similar ambient conditions so these values will be used throughout this work. The Reynolds number was calculated using the equation,  $Re = \rho VL / \mu$  where  $V$  is the mean velocity of an object relative to air,  $L$  is the characteristic length, and  $\mu = 1.79 \times 10^{-5} \text{ kg m}^{-1} \text{ s}^{-1}$  is the dynamic viscosity of air. For the cube,  $L$  was the side of the cube. For the sphere, the Reynolds number equation is defined as  $Re = \rho Vd / \mu$ , where  $d$  is the diameter of the sphere.

Velocity profiles of the test section in the miniature wind tunnel were measured by using the pitot-static probe and differential pressure manometer. Before the tests, 15

divisions, with 5 mm spacing, were marked on the probe. The pitot-static probe was then lowered into the test section and the total and static pressure ports were connected to the differential pressure manometer using silicone tubing. Before the test, the approximate value of the expected differential pressure for a desired velocity was calculated using the Bernoulli's equation, which was done for all velocities. The fan was then turned on and the differential pressure readings were noted for each velocity at different section locations by moving the probe vertically using the markings on the probe for reference. The hot-wire anemometer was also used at the same time to confirm the readings displayed on the differential pressure manometer up to the capacity of the anemometer which was  $20+ \text{ m s}^{-1}$ . A typical upstream velocity profile with the miniature wind tunnel operating at  $20 \text{ m s}^{-1}$  is shown in Figure 2.6.

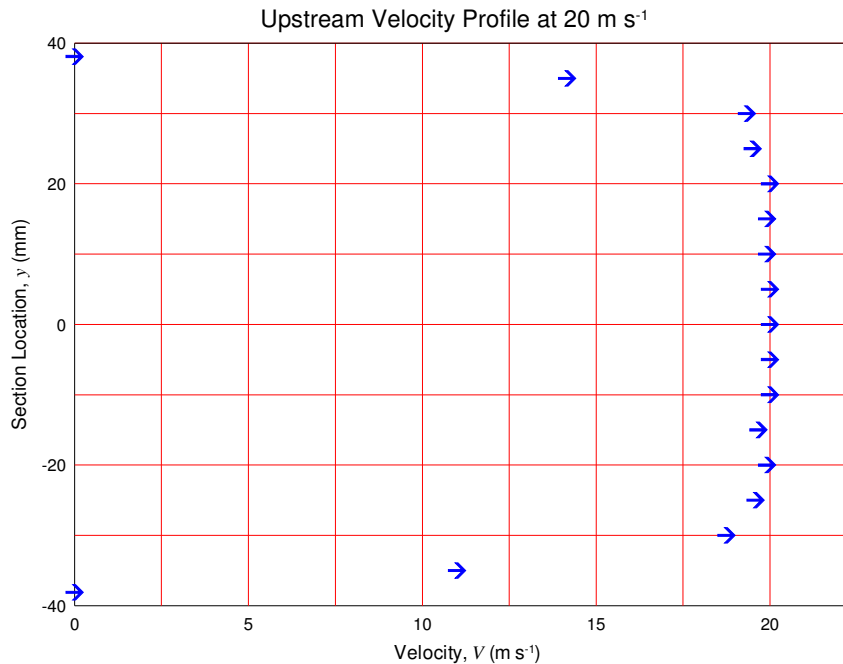


Figure 2.6. Velocity Profile of Test Section at  $20 \text{ m s}^{-1}$ .  
*At the pitot-static probe location, velocities were relatively constant through the center portion of the section.*

Drag coefficient ( $C_D$ ) estimates were made using the equation

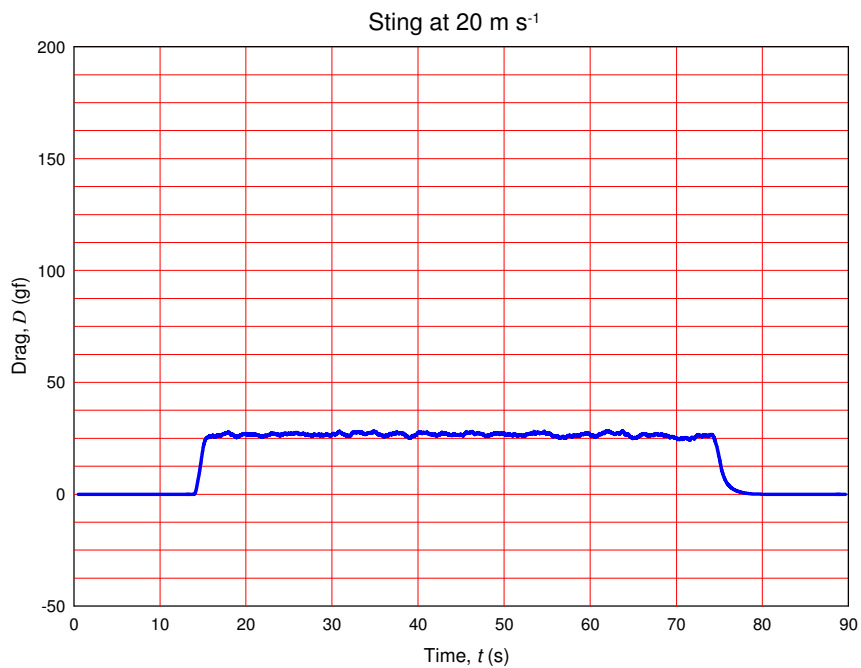
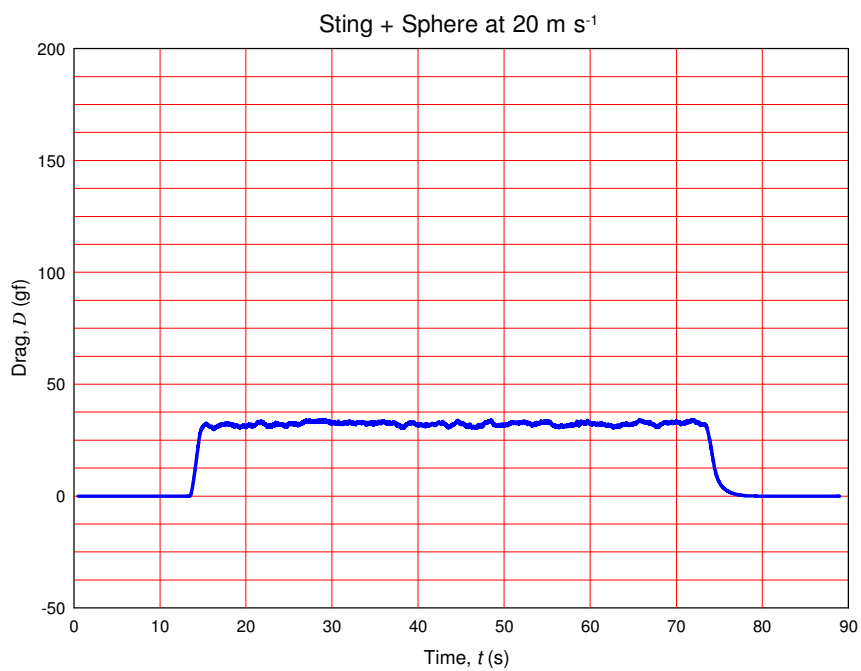
$$C_D = \frac{D}{\frac{1}{2}\rho V_\infty^2 S} \quad (2)$$

where  $D$  is the drag force in gf and  $V_\infty$  is the freestream velocity in  $\text{m s}^{-1}$ . The calculated  $S$  for Sphere and Cube were shown in Table 2.2. Actual test model drag was found by subtracting the tare using the “Sting only” drag from the “Sting + Model” drag. The tests were performed according to the steps discussed earlier. Typical drag measurements with the wind tunnel operating at  $20 \text{ m s}^{-1}$  are shown in Figs. 2.7 to 2.9. The running average of the data, 101 point moving average, is shown in blue. Because the drag force data has been obtained by running average, the drag for all test objects are averaged values of  $D$  over a period of  $T = 50$  seconds beginning at 20 seconds. The equation for average drag ( $\bar{D}$ ) is given as

$$\bar{D} = \frac{1}{T} \int_0^T D(t) dt \quad (3)$$

where  $t$  is time. The average drag coefficient for each test model is then obtained as follows

$$\bar{C}_D = \frac{\bar{D}}{\frac{1}{2}\rho V_\infty^2 S} \quad (4)$$

Figure 2.7. Sting at 20 m s<sup>-1</sup>.Figure 2.8. Sting + Sphere at 20 m s<sup>-1</sup>.

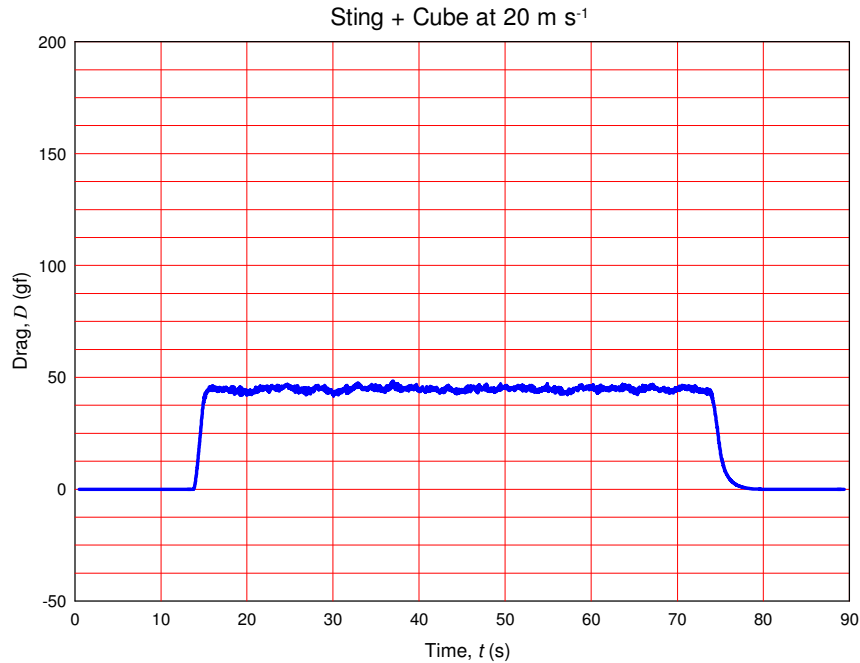


Figure 2.9. Sting + Cube at 20 m s<sup>-1</sup>.

#### *Example $C_D$ Calculations*

The  $\bar{D}$  value of the Sting was subtracted from the  $\bar{D}$  value of Sting-Model configuration to estimate the corrected average drag force of both test models. An example average drag coefficient calculation is shown below for 20 m s<sup>-1</sup>.

a)  $\bar{C}_D$  of Sphere at 20 m s<sup>-1</sup>

$$\bar{D} \text{ of Sting-Sphere configuration} = 32.28 \text{ gf}$$

$$\bar{D} \text{ of Sting} = 26.71 \text{ gf}$$

$$\bar{D} \text{ of Sphere} \approx 32.28 \text{ gf} - 26.71 \text{ gf}$$

$$\approx 5.57 \text{ gf}$$

$$\approx 0.0546 \text{ N}$$

$$\overline{C_{D\ Sphere}} = \frac{\overline{D}}{\frac{1}{2}\rho V_{\infty}^2 S} = \frac{0.0546 \text{ N}}{\frac{1}{2}(1.2 \text{ kg/m}^3)(20 \text{ m/s})^2(5.07 \times 10^{-4} \text{ m}^2)}$$

$$\overline{C_{D\ Sphere}} \approx 0.44$$

b)  $\overline{C_D}$  of Cube at  $20 \text{ m s}^{-1}$

$$\overline{D} \text{ of Sting-Cube configuration} = 44.79 \text{ gf}$$

$$\overline{D} \text{ of Sting} = 26.71 \text{ gf}$$

$$\overline{D} \text{ of Cube} \approx 44.79 \text{ gf} - 26.71 \text{ gf}$$

$$\approx 18.08 \text{ gf}$$

$$\approx 0.1773 \text{ N}$$

$$\overline{C_{D\ Cube}} = \frac{\overline{D}}{\frac{1}{2}\rho V_{\infty}^2 S} = \frac{0.1773 \text{ N}}{\frac{1}{2}(1.2 \text{ kg/m}^3)(20 \text{ m/s})^2(6.60 \times 10^{-4} \text{ m}^2)}$$

$$\overline{C_{D\ Cube}} \approx 1.12$$

Tables 2.3 and 2.4 show the average drag coefficients of Sphere and Cube for a range of Reynolds numbers.



Table 2.3. Average Drag Coefficient of Sphere.

Reynolds number ( $Re$ )	Average Drag Coefficient ( $\overline{C_D}$ )
$8.5 \times 10^3$	0.53
$1.7 \times 10^4$	0.49
$2.5 \times 10^4$	0.44
$3.4 \times 10^4$	0.44
$4.2 \times 10^4$	0.48
$5.1 \times 10^4$	0.46

Table 2.4. Average Drag Coefficient of Cube.

Reynolds number ( $Re$ )	Average Drag Coefficient ( $\overline{C_D}$ )
$8.6 \times 10^3$	1.40
$1.7 \times 10^4$	1.27
$2.6 \times 10^4$	1.23
$3.5 \times 10^4$	1.12
$4.3 \times 10^4$	1.19
$5.2 \times 10^4$	1.25

The drag coefficients for the Sphere and Cube were close to published values of 0.47 and 1.05 shown in Figure 2.10. A plot of Average Drag Coefficient versus Reynolds number is shown in Figure 2.11. The measured  $\overline{C_D}$  of the Sphere closely follows the published values as shown in Figure 2.12.















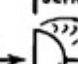







3-Dimension			2-Dimension		
SHAPE	REF.	$C_D$	SHAPE	REF.	$C_D$
	STRING SUPPORT	0.47 <sub>y</sub>		—	1.17 <sub>y</sub>
	(c)	0.38		(a)	1.20
	(c)	0.42		(g)	1.16
	(e)	0.59 <sub>y</sub>		(d)	1.60 <sub>y</sub>
	(f)	0.80 <sub>y</sub>		(e)	1.55
	(d)	0.50		(a)	1.55
	SEPARATION	1.17		VORTEX STREET	1.98
	(c)	1.17		(a)	2.00
	(b)	1.42		(a)	2.30
	(a)	1.38		(b)	2.20
	(f)	1.05 <sub>y</sub>		(a)	2.05 <sub>y</sub>

Figure. 2.10. Drag Coefficients of Various Shapes [35].

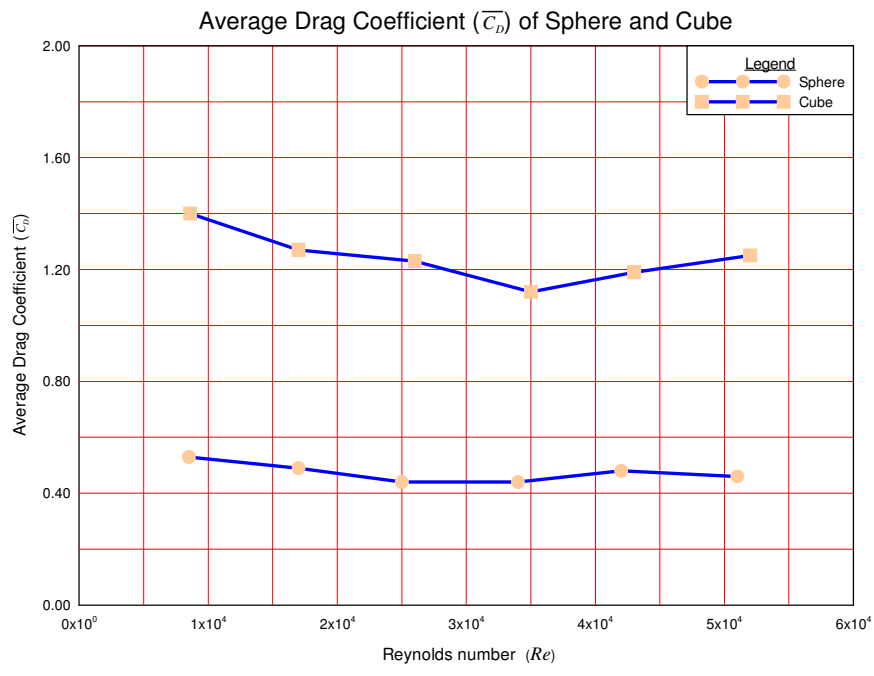


Figure 2.11. Average Drag Coefficient of Sphere and Cube Versus Reynolds number.

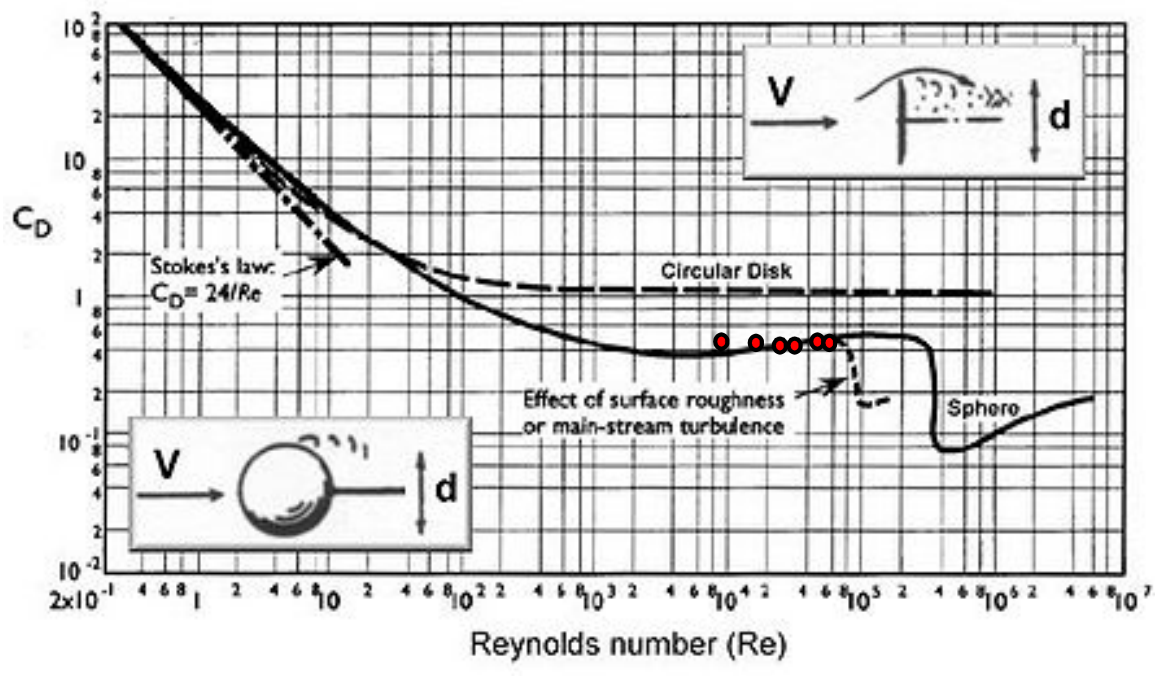


Figure. 2.12. Drag Coefficient of Smooth Sphere [36].  
The red dots on the graph indicate the measured drag coefficient values of the Sphere test model in the miniature wind tunnel.

Small fluctuations in the differential pressure manometer readings showed that the airflow was essentially smooth and turbulence free. The Sphere and Cube dimensions were chosen to be small to avoid flow interference with the test section walls and/or interaction with the boundary layer, which can lead to erroneous results.

Compared to wind tunnels with rectangular test sections, the cylindrical geometry was much easier to fabricate for a quality flow. Although, during fabrication, difficulties were encountered when trying to minimize “aerodynamic noise”, which was sensed by the high fidelity load cell (strain gauge type instruments can be very sensitive to dynamic fluctuations).

The overall fabrication cost (excluding the load cell and data acquisition system) was in the neighborhood of \$1,000. Many readily available parts were used. Miniature wind tunnels of this type are simple and easy to use, require low power, and employ small test models that can be purchased or quickly made, possibly through rapid prototyping or other means.

The average drag coefficient of Sphere and Cube were used to validate the miniature wind tunnel, and the values were consistent with the published results over the range of test Reynolds numbers. Therefore, the results obtained lend confidence that the tunnel can be used to study the effects of the surface finish on the drag of various models at low speeds.

## **Chapter 3**

### **Ribbed Fabric Experiments**

The current chapter describes the results from the experiments that were performed. The goals of the experiments were to test NACA 0012 wing models at zero incidence with fabrics as surface finishes or “skins” so as to determine the effects, if any, on boundary layer skin friction drag. First, a preliminary series of tests was conducted over a limited range of wind speeds and chord Reynolds numbers on fourteen different fabrics; three fabrics were chosen for further study based on the outcome that they showed the lowest drag force values. Wing models with a smooth surface and with a boundary layer trip were used as a baseline for comparisons of the drag force with the fabric test models. Second, a series of tests was conducted over a wider range of Reynolds numbers and the drag coefficients of the fabrics were compared with the baseline cases to determine any drag reduction.

#### **3.1 Preliminary Fabric Test**

Grooved or “riblet” like surface structures similar to those on Speedo® Fastskin® FSI swimsuit fabric were investigated. A total of fourteen different fabric types, each having distinct riblet like patterns, was purchased. A Speedo® Fastskin® FSI swimsuit was also purchased for comparison. Although used in water, this fabric is hydrophobic, often contacts air, thus creating a variety of boundary layer conditions.

To fabricate the test models for drag measurement, an EPS (expanded polystyrene) foam wing of NACA 0012 configuration with 15.2 cm chord (6 in) and total span of

182.9 cm (72 in) was obtained. Several wing test models were dry cut using a sectioning machine to obtain wingspans that were approximately 5.1 cm (2 in). Slightly less than 0.25 in diameter holes were drilled into each small wing, through the chord line, starting from the trailing edge. A round brass tube with 9/32 in OD and 0.253 in ID was pressed into the drilled hole for mounting onto the sting. The exit of the tube was compressed in a screw driven machine between aluminum blocks to fit within the trailing edge. Foam fill was sprayed into the depression created by the sting mounting tube, allowed to cure, and then sanded to maintain the NACA 0012 profile shape.

Each fabric was cut to a length of about 30.5 cm (12 in) and width of about 5.1 cm (2 in). Spray adhesive was applied on the upper and lower surfaces of the wing model. After waiting for about 1 min, the fabric was carefully laid on the entire surface of the model and smoothed by hand to ensure that no bubbles were present between the fabric and underlying EPS. This method was repeated for all of the fourteen wing test models. Figure 3.1 shows the wing models with fabric skins. Figures 3.2 to 3.15 show details of the weave pattern for each fabric; the direction of airflow is from top to bottom.



Figure 3.1. NACA 0012 Wing Models with Fabrics.  
 (a) Navy Blue; (b) Fastskin<sup>®</sup> FSI; (c) Purple; (d) Pattern; (e) Beige Thin; (f) Diamond;  
 (g) Sky Blue; (h) Black; (i) Light Pink; (j) Corduroy; (k) Beige Thick; (l) Herringbone;  
 (m) Gold; (n) Purple Stripe.



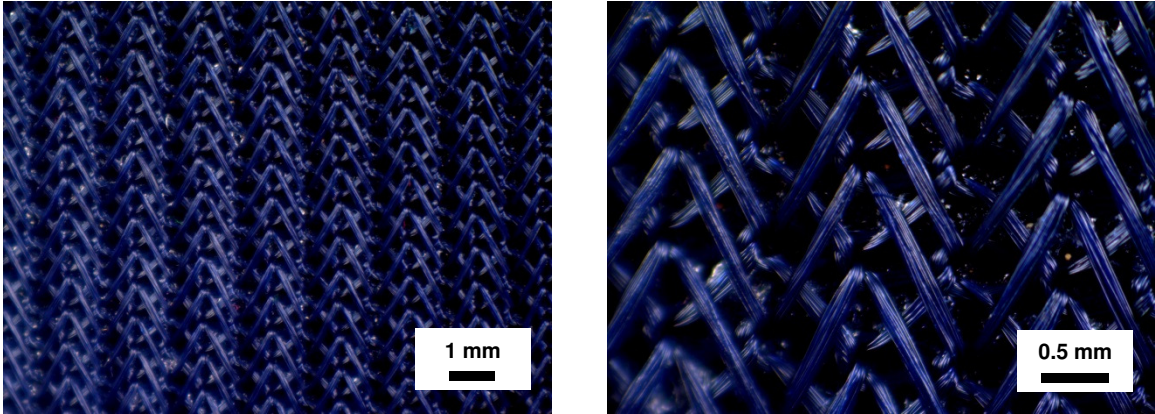


Figure 3.2. Navy Blue.

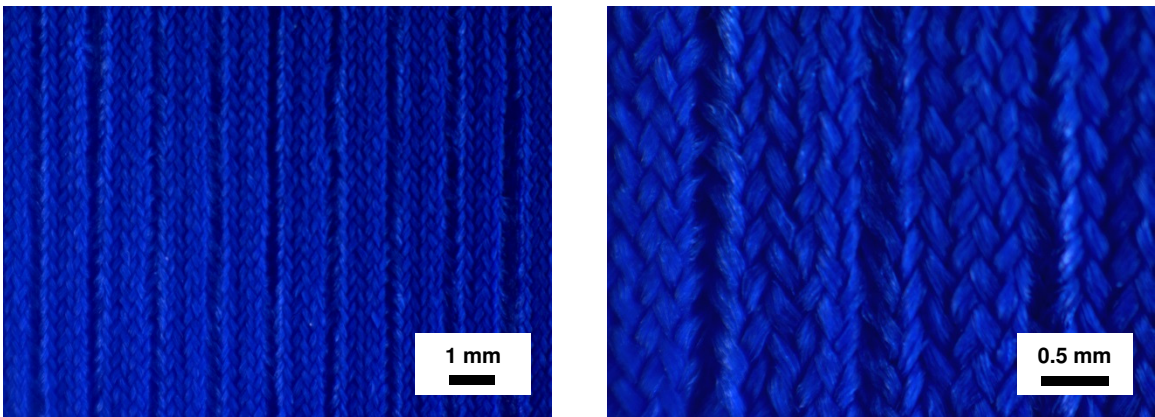


Figure 3.3. Fastskin® FSI.

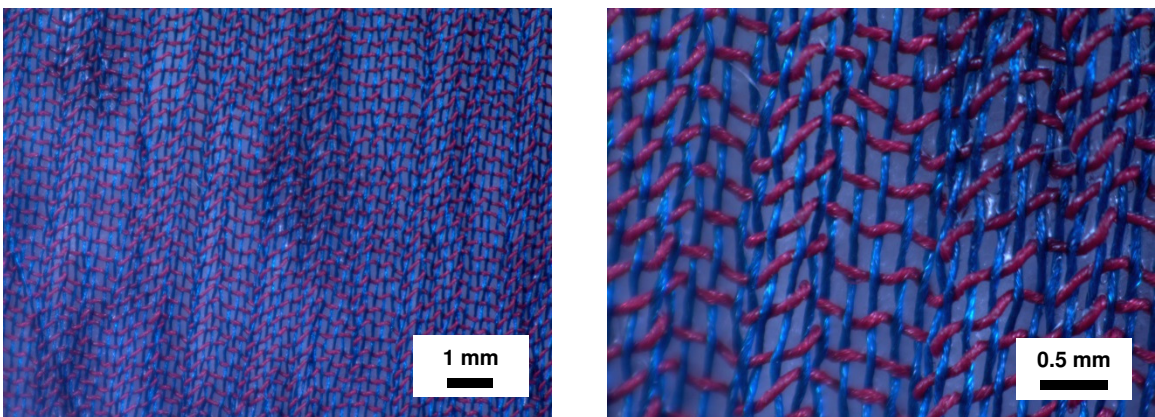


Figure 3.4. Purple.



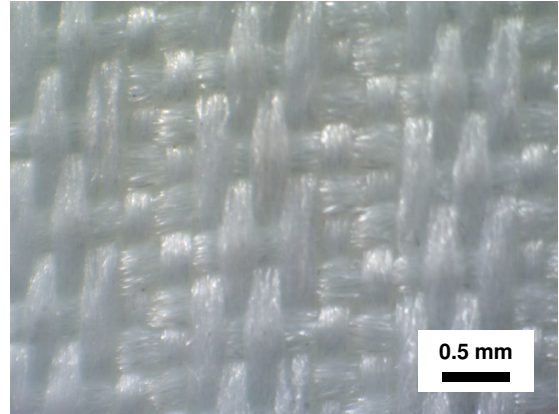
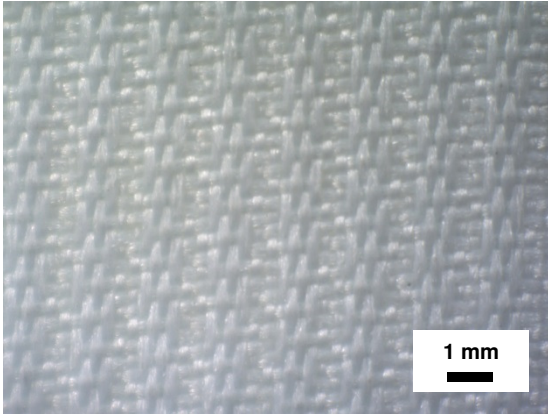


Figure 3.5. Pattern.

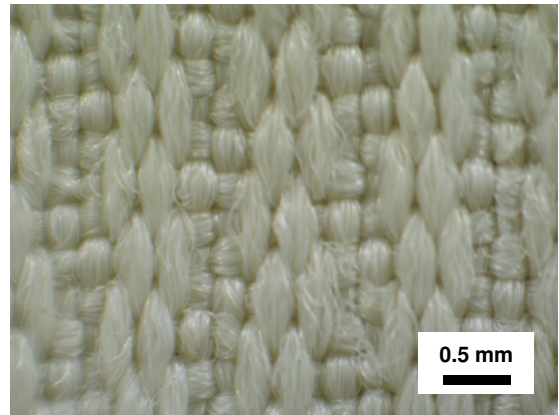
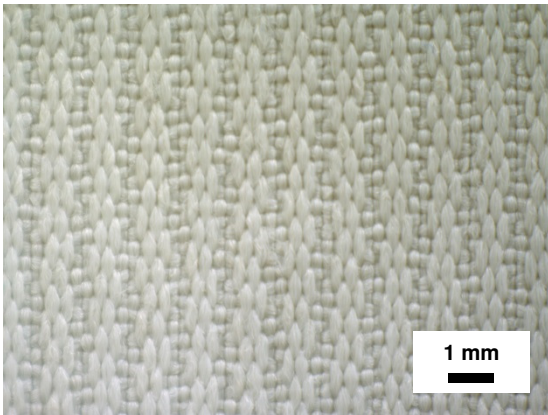


Figure 3.6. Beige Thin.

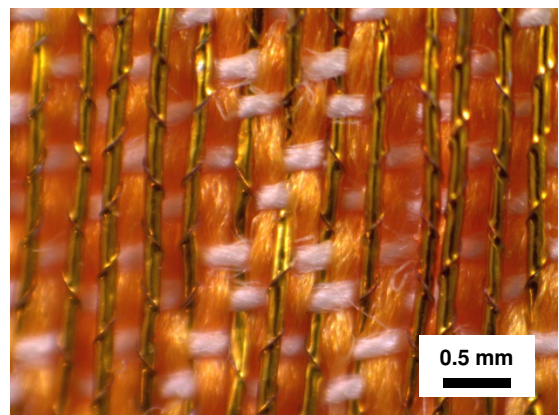
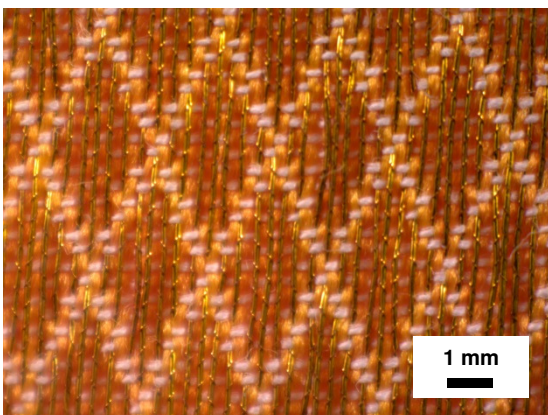


Figure 3.7. Diamond.

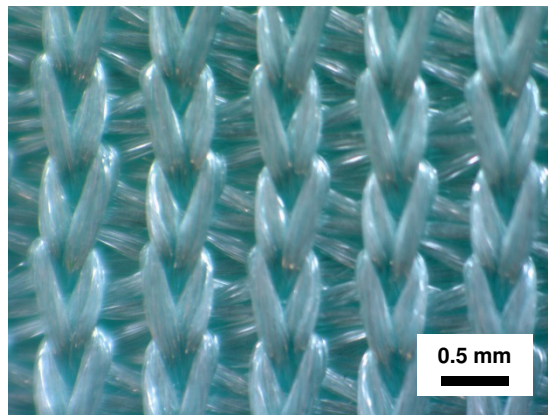
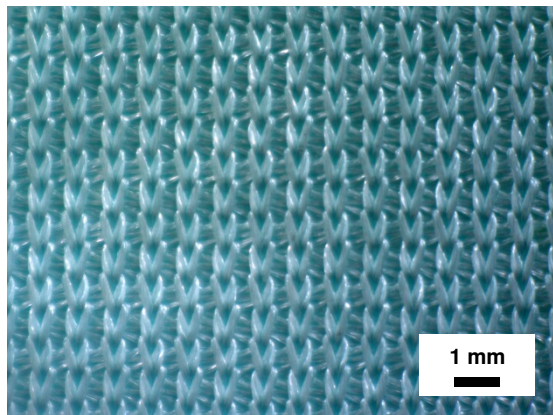


Figure 3.8. Sky Blue.

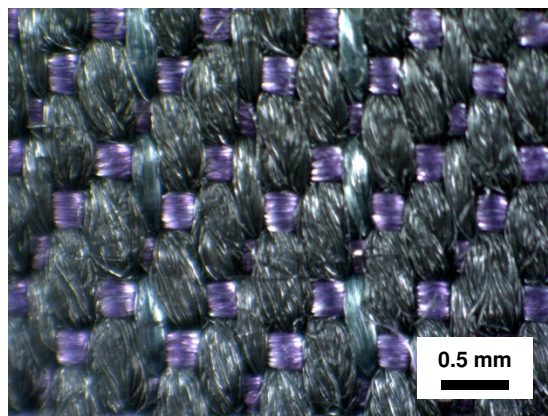
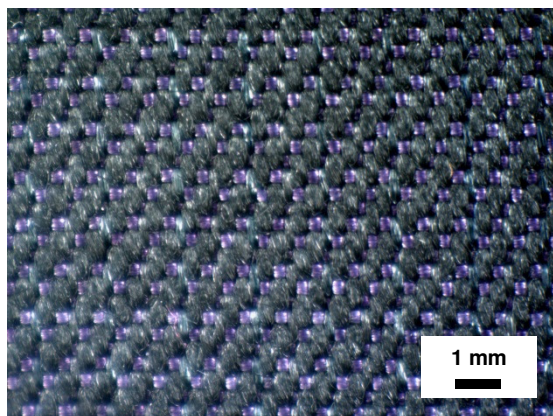


Figure 3.9. Black.

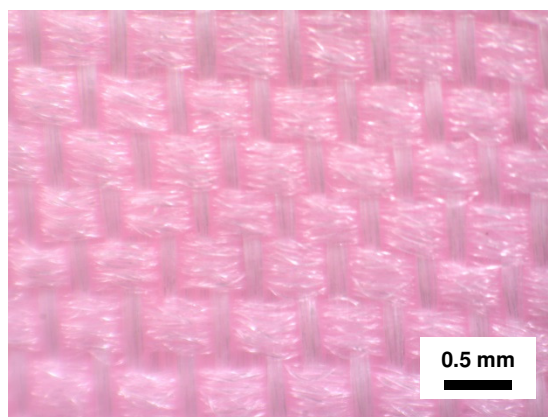
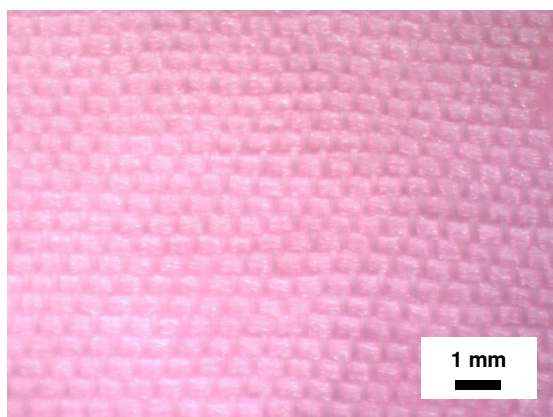


Figure 3.10. Light Pink.



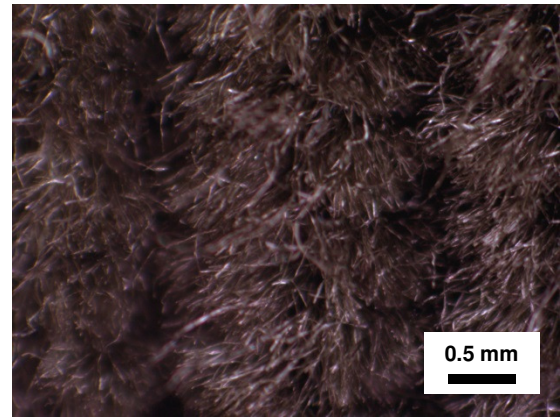
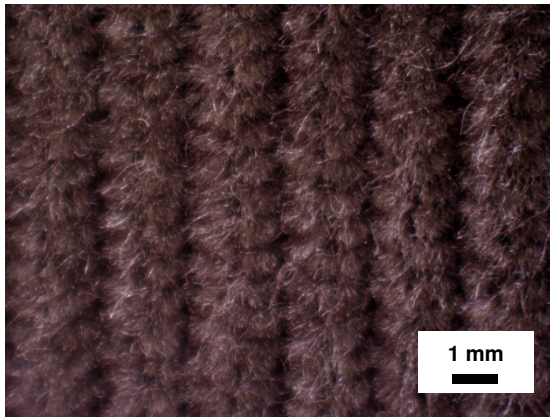


Figure 3.11. Corduroy.

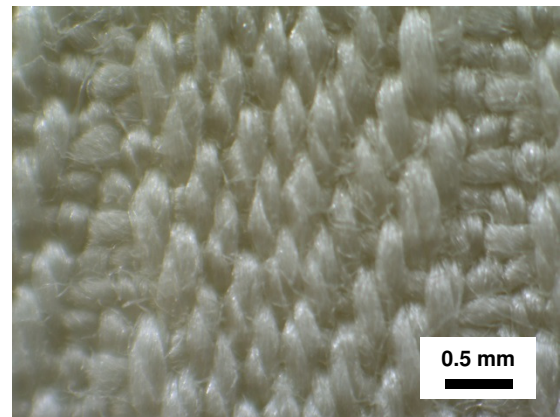
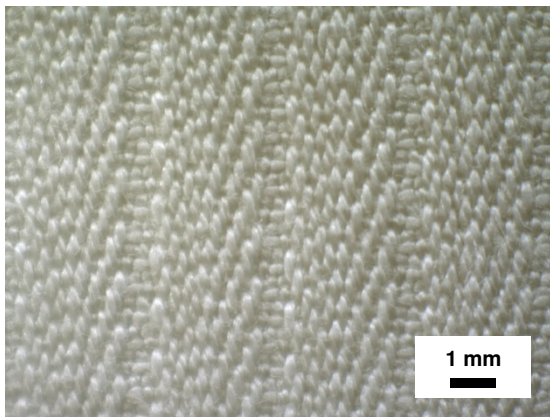


Figure 3.12. Beige Thick.

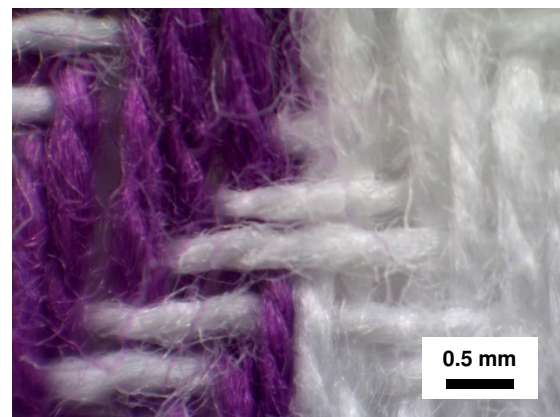
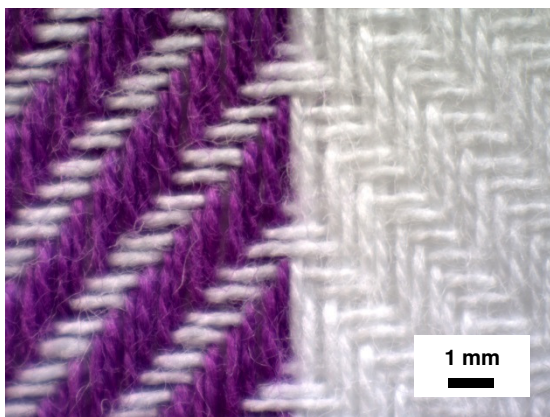


Figure 3.13. Herringbone.

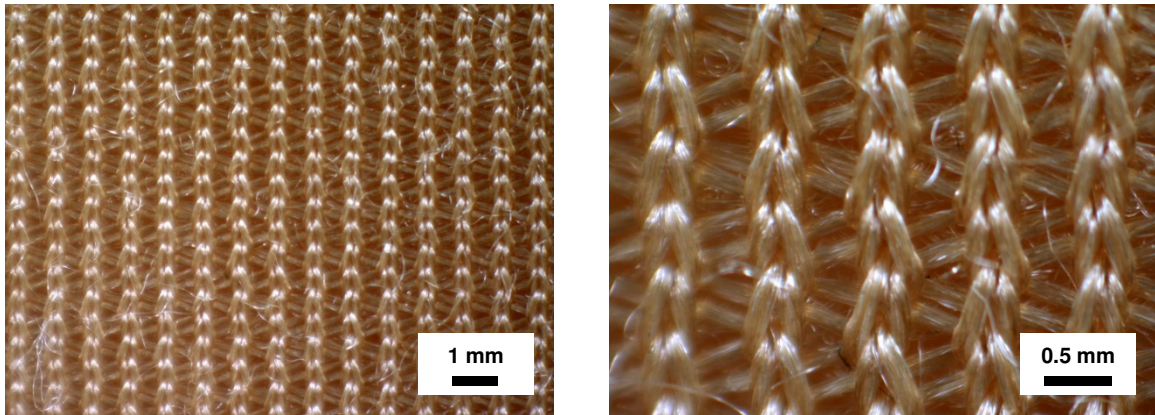


Figure 3.14. Gold.

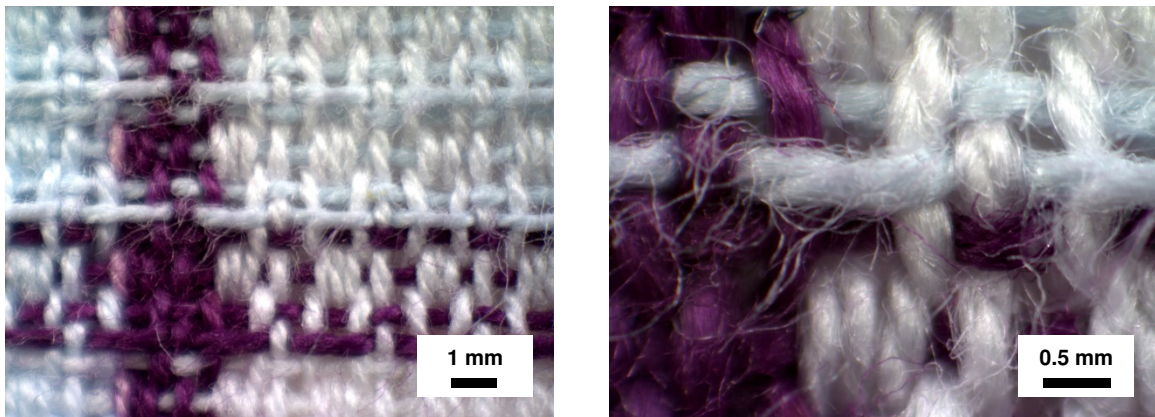


Figure 3.15. Purple Stripe.

All fourteen wing models with fabric skins were tested. These tests were performed to eliminate fabrics that had much higher  $\overline{C_D}$  values so as to choose the best fabrics for a final set of more detailed tests. The chord Reynolds number was calculated using the equation  $Re = \rho Vc / \mu$  where  $c$  is the chord of the wing model. Average drag coefficient of each fabric was calculated for all wind speeds using the average drag force for each wing model and the average drag coefficient equation, i.e., Eqns. (3) and (4). Table 3.1 shows the  $\overline{C_D}$  for all fourteen fabric skin wing models at  $5 \text{ m s}^{-1}$ ,  $10 \text{ m s}^{-1}$  and  $15 \text{ m s}^{-1}$ .

Table 3.1.1. Average Drag Coefficient of Preliminary Fabric Test.

$V$ (m/s)	$Re$	$\overline{C_D}$													
		Navy Blue	Fastskin FSI	Purple	Pattern	Beige Thin	Diamond	Sky Blue	Black	Light Pink	Corduroy	Beige Thick	Herring bone	Gold	Purple Stripe
5	$5.11 \times 10^4$	0.0694	0.1036	0.0796	0.0899	0.0993	0.0964	0.1090	0.1248	0.1152	0.0972	0.1365	0.1207	0.1559	0.1752
10	$1.02 \times 10^5$	0.0404	0.0221	0.0431	0.0447	0.0547	0.0517	0.0526	0.0480	0.0601	0.0856	0.0668	0.0849	0.0920	0.1157
15	$1.53 \times 10^5$	0.0484	0.0510	0.0572	0.0500	0.0467	0.0625	0.0529	0.0591	0.0531	0.0879	0.0749	0.0926	0.0900	0.1055

From Table 3.1 it can be seen that the fabric identified as Navy Blue generally had the lowest values of  $\overline{C_D}$  (indicated as dark green), and the fabric identified by Purple Stripe generally had the highest values of  $\overline{C_D}$  (indicated as bright red). For the final fabric test, Fastskin<sup>®</sup> FSI was selected as its  $\overline{C_D}$  values were consistently low for all wind speeds. The fabric identified as Beige Thin was also chosen for the final fabric test as its  $\overline{C_D}$  value was the lowest at 15 m s<sup>-1</sup>. The Herringbone was also of interest as this is a common composite reinforcement weave. For the final fabric test, models with the chosen fabric skins as well as a smooth 2024-T3 aluminum skin were carefully fabricated using a slightly different approach.

### 3.2 Final Fabric Test

To confirm the above preliminary results, four EPS foam wing models of NACA 0012 configuration were dry cut to obtain wingspans of 7.6 cm (3 in). The holes were drilled and the sting mounting tube was inserted into the models by the same procedure as described earlier. A sheet of 0.030 cm (0.012 in) thick 2024-T3 aluminum was cut to a length that was more than 30.5 cm (12 in) and width of 7.6 cm (3 in). The sheet was then carefully bent to obtain the leading edge curvature of the NACA 0012 wing configuration. Two part epoxy adhesive was mixed and uniformly applied onto the EPS core, then the aluminum sheet was laid onto the core starting with the leading edge and applying pressure to cover the entire surface. Maintaining pressure, the epoxy was allowed to cure overnight, and then the model was carefully wet (tap water) cut using the sectioning machine to obtain a wingspan of very close to 5.1 cm (2 in). This wet cut



process cooled and washed away any extra pieces of aluminum sticking to the wing model and ensured that both sides were smooth.

Models with Fastskin<sup>®</sup> FSI, Beige Thin, and the Herringbone were also prepared in a similar way using spray adhesive however these were dry cut so that the fabrics would not be contaminated. Figure 3.16 shows the final 2024-T3 aluminum, Fastskin<sup>®</sup> FSI, Beige Thin, and Herringbone wing test models.

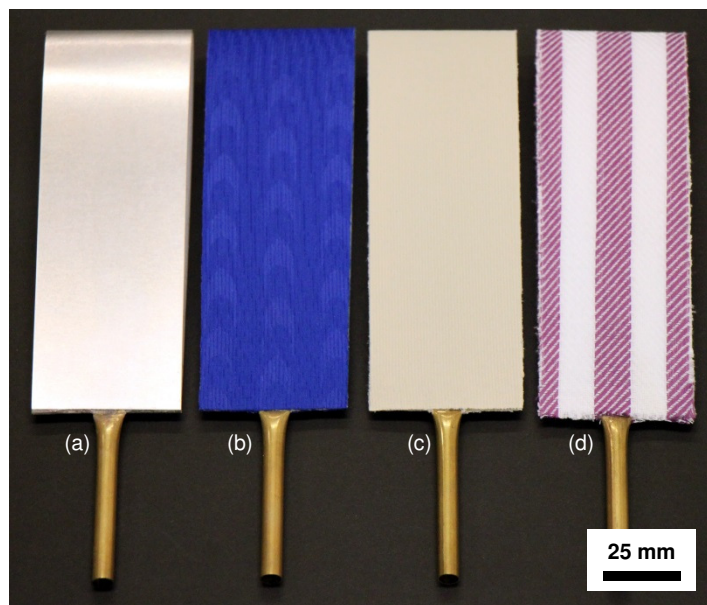
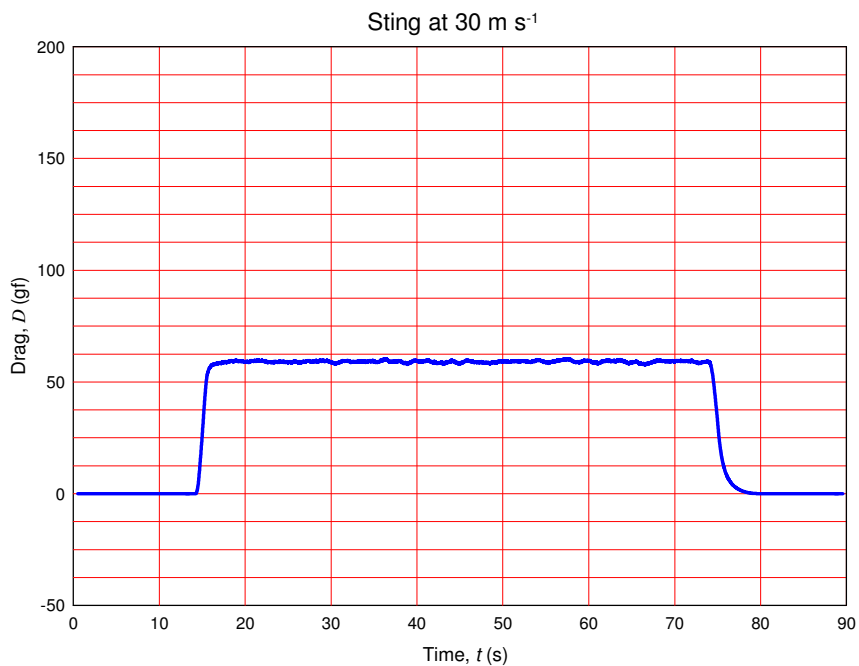
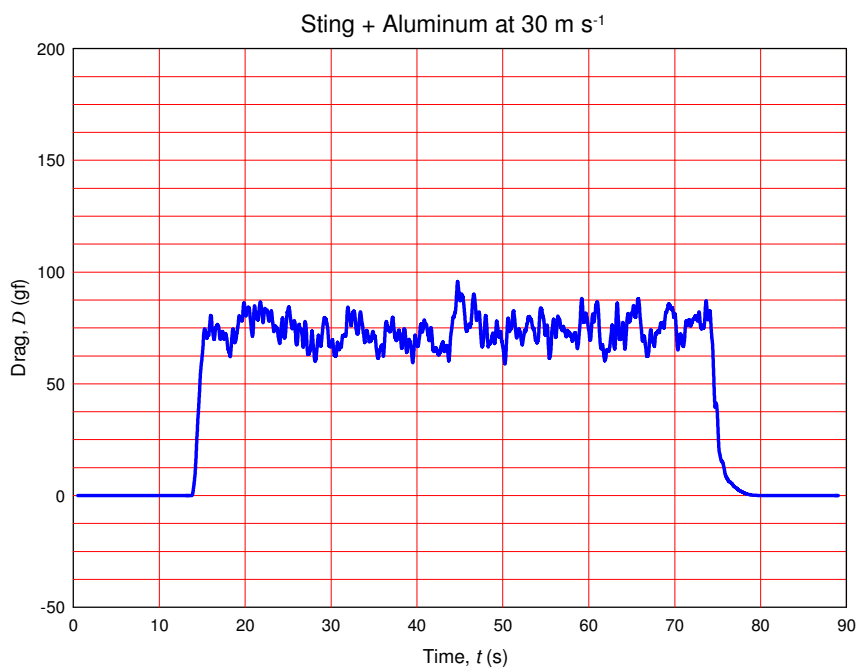


Fig. 3.16. Final Wing Test Models.  
(a) 2024-T3 aluminum; (b) Fastskin<sup>®</sup> FSI; (c) Beige Thin; (d) Herringbone.

All of the wing test models were mounted in the wind tunnel and tested at wind speeds of  $5 \text{ m s}^{-1}$ ,  $10 \text{ m s}^{-1}$ ,  $15 \text{ m s}^{-1}$ ,  $20 \text{ m s}^{-1}$ ,  $25 \text{ m s}^{-1}$ , and  $30 \text{ m s}^{-1}$ . Representative drag measurement plots for the sting only and the four wing test models with the wind tunnel operating at  $30 \text{ m s}^{-1}$  are shown in Figs. 3.17 to 3.21.

Figure 3.17. Sting at 30 m s<sup>-1</sup>.Figure 3.18. Sting + Aluminum at 30 m s<sup>-1</sup>.



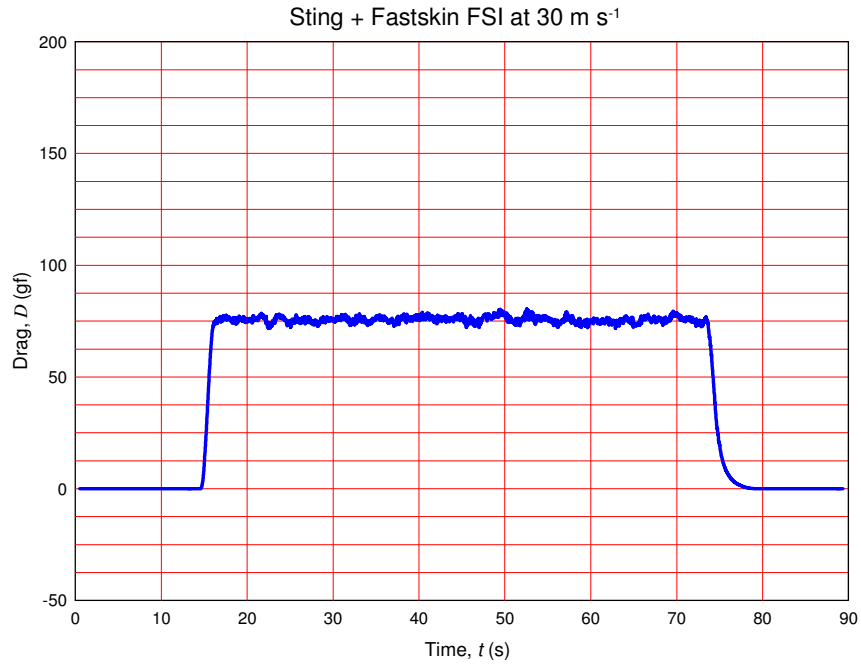


Figure 3.19. Sting + Fastskin<sup>®</sup> FSI at 30 m s<sup>-1</sup>.

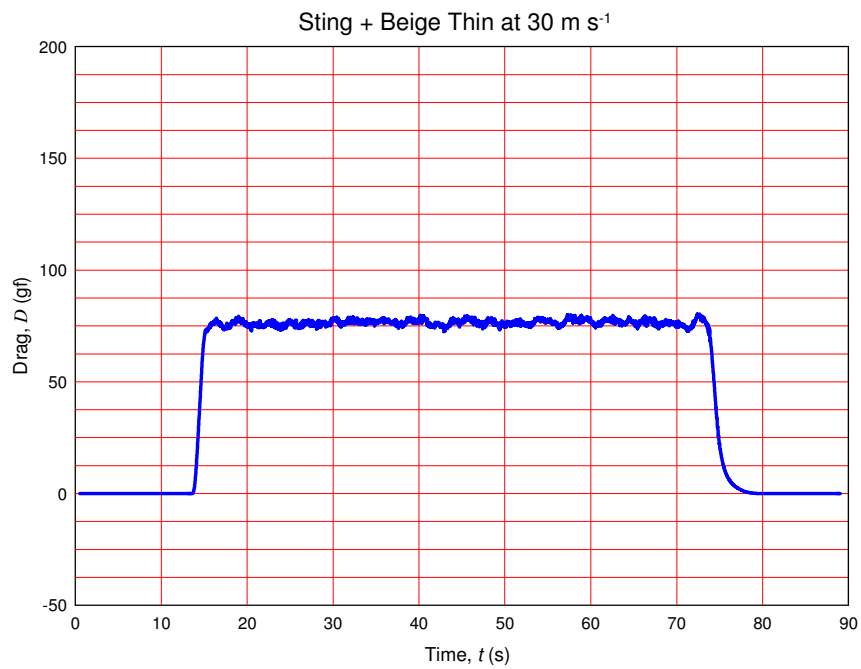


Figure 3.20. Sting + Beige Thin at 30 m s<sup>-1</sup>.

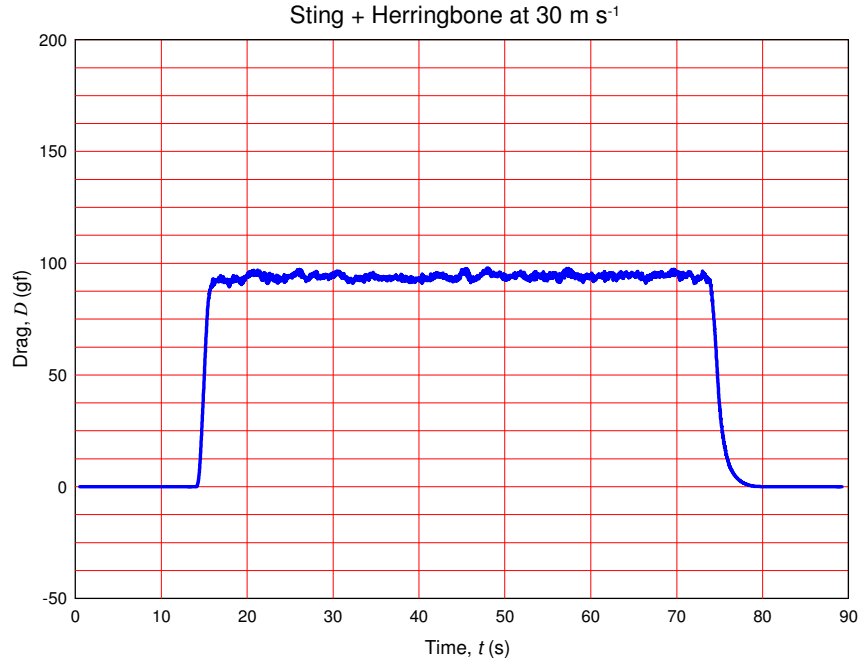


Figure 3.21. Sting + Herringbone at  $30 \text{ m s}^{-1}$ .

Average drag coefficient of four wing models was calculated for all six velocities.

Table 3.2 shows the  $\overline{C_D}$  data for the final fabric test.

Table 3.2. Average Drag Coefficient of Final Fabric Test.

		$\overline{C_D}$			
$V$ (m/s)	$Re$	Aluminum	Fastskin FSI	Beige Thin	Herring bone
5	$5.11 \times 10^4$	0.0802	0.0741	0.0731	0.1032
10	$1.02 \times 10^5$	0.0484	0.0521	0.0497	0.0998
15	$1.53 \times 10^5$	0.0451	0.0423	0.0442	0.0881
20	$2.04 \times 10^5$	0.0386	0.0423	0.0476	0.0918
25	$2.55 \times 10^5$	0.0304	0.0403	0.0441	0.0847
30	$3.07 \times 10^5$	0.0360	0.0402	0.0416	0.0837

From Table 3.2, it can be seen that the smooth aluminum surface had the lowest value of  $\overline{C_D}$  (indicated as dark green) and Herringbone had the highest value of  $\overline{C_D}$  (indicated as bright red) at all wind speeds. Fastskin® FSI performed slightly better than Beige Thin and much better than Herringbone. Note the presence of vibrations with the aluminum skinned model as compared to the others. Some researchers have mentioned a beneficial quieting effect with riblets. Walsh [10] discusses noise, vibration and flutter caused by turbulence and suggests the use of riblets as a means of damping.

The aluminum wing model used in this test was smooth and at the low chord Reynolds number test range, can be expected to have extensive regions of laminar flow on its surface. However, the roughness of the skins or riblet-like materials will generally cause almost immediate transition from the laminar to a turbulent boundary layer profile, so the best basis for comparison is a smooth airfoil but with a turbulent boundary layer over its entire surface from leading edge to trailing edge. At the low Reynolds numbers of the present tests, it is not possible to generate a turbulent boundary layer of prescribed thickness by relying on natural transition. However, the use of a boundary layer leading edge trip is common experimental practice [37] and the trip causes transition to turbulence at low Reynolds number while increasing the boundary layer thickness by the thickness of the wake downstream of the trip. The idea of the trip is simulate the development of a naturally developing turbulent boundary layer, although caution needs to be used so that the trip does not cause separation of the laminar boundary layer or the creation of an artificially thick turbulent boundary layer.

First, the smooth aluminum wing model was modified by standardizing the roughness on its surface. Both the upper and lower surface of the wing model was dry

sanded in a chordwise direction using 600 grit SiC sandpaper. Second, a boundary layer trip strip was applied at the leading edge of the airfoil on both the upper and lower surfaces.

The trips were made first by using two strips of tape about 2 mm apart. A thin layer of quick-setting epoxy was carefully coated between the strips and Ottawa sand, which is mostly spherical sand particles of about 100 microns in diameter, was sprinkled over the adhesive. Extra sand particles were brushed off from the surface. After waiting for half-hour, the tapes were carefully peeled away to expose the boundary layer trip strip, which was between 100 and 200 microns thick. The same procedure was followed for the lower surface of the wing model.

Figures 3.22a and 3.22b show photographs of the aluminum wing model with the boundary layer trip strip. The wing model was tested in the wind tunnel at the same wind speeds. Figure 3.23 shows the drag measurement plot for the aluminum wing model with the boundary layer trip strip. Table 3.3 shows the average drag coefficient data.



Figure 3.22a. Aluminum Wing Model with Boundary Layer Trip Strip (side view).  
*For the wing model, the span is  $\sim 5.1$  cm (2 in) and the chord is  $\sim 15.2$  cm (6 in).*

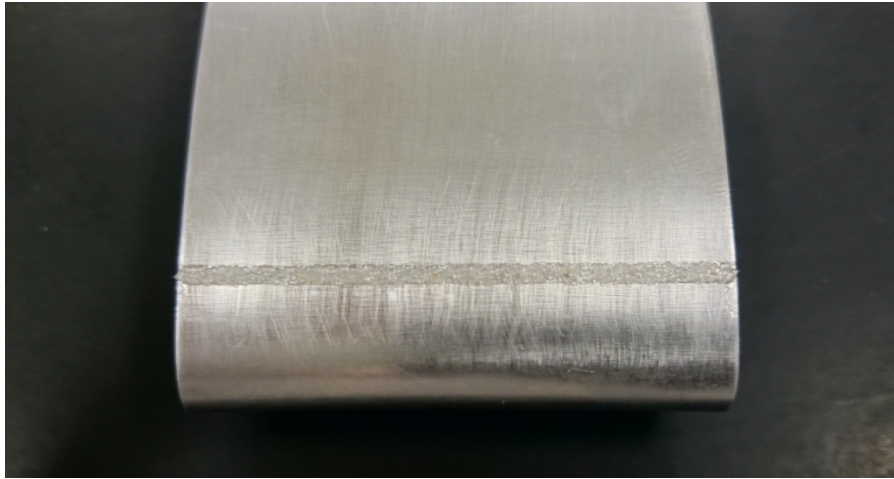


Figure 3.22b. Aluminum Wing Model with Boundary Layer Trip Strip (front view).  
*The span of the wing model is  $\sim 5.1$  cm (2 in).*

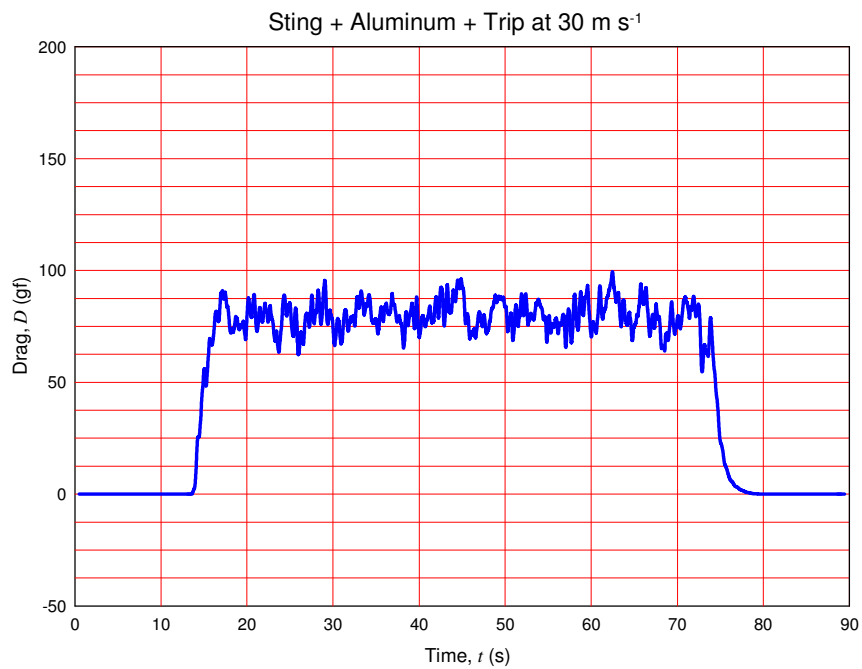


Figure 3.23. Sting + Aluminum + Trip at  $30 \text{ m s}^{-1}$ .

Table 3.3. Average Drag Coefficient of Aluminum + Trip.

$V$ (m/s)	$\overline{C_D}$ Aluminum + Trip
5	0.0471
10	0.0484
15	0.0467
20	0.0504
25	0.0513
30	0.0506

To compare the performance of the fabric skins with the aluminum wing model with boundary layer trip, a difference or “delta” of the average drag coefficient values was calculated by using the equation

$$\Delta \overline{C_D} = \overline{C_{D \text{ Fabric}}} - \overline{C_{D \text{ Aluminum + Trip}}} \quad (5)$$

$\overline{\Delta C_D}$  was calculated for all fourteen fabric wing models in the preliminary fabric test. Figures 3.23a to 3.23e shows the plot of delta average drag coefficient ( $\overline{\Delta C_D}$ ) versus Reynolds number ( $Re$ ).

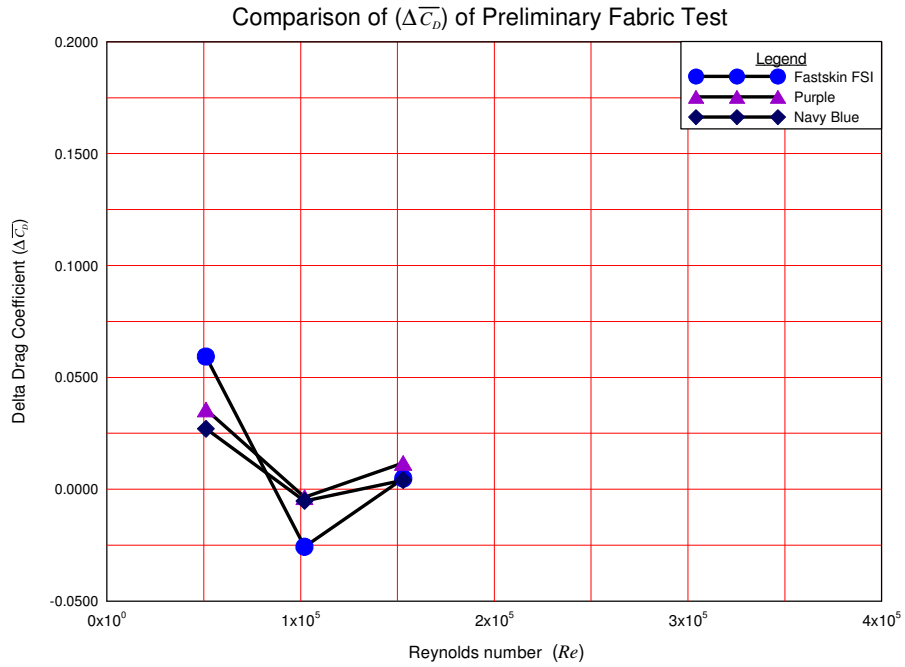


Figure 3.24a. Delta Average Drag Coefficient of Preliminary Fabric Test.

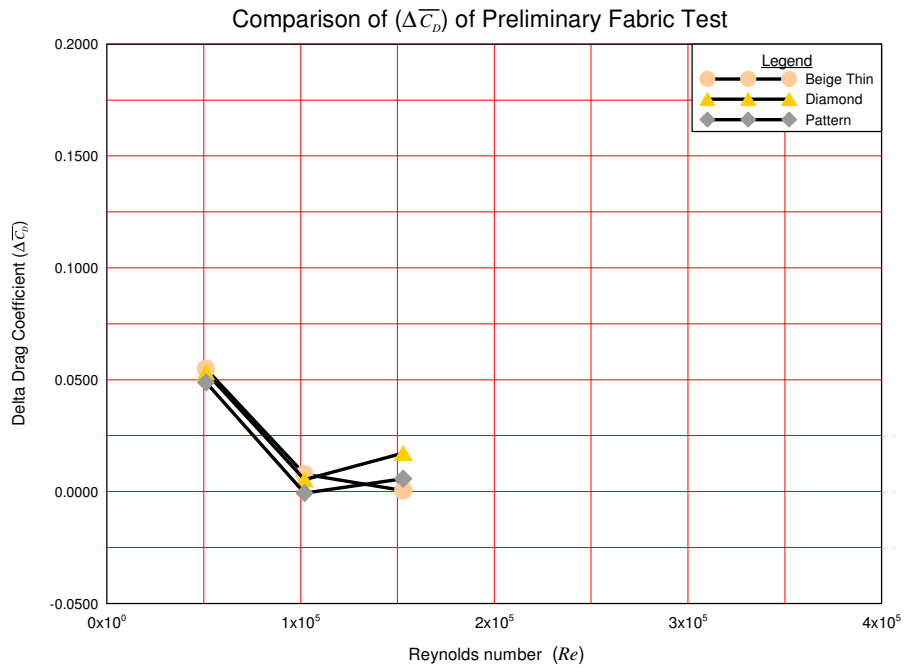


Figure 3.24b. Delta Average Drag Coefficient of Preliminary Fabric Test.

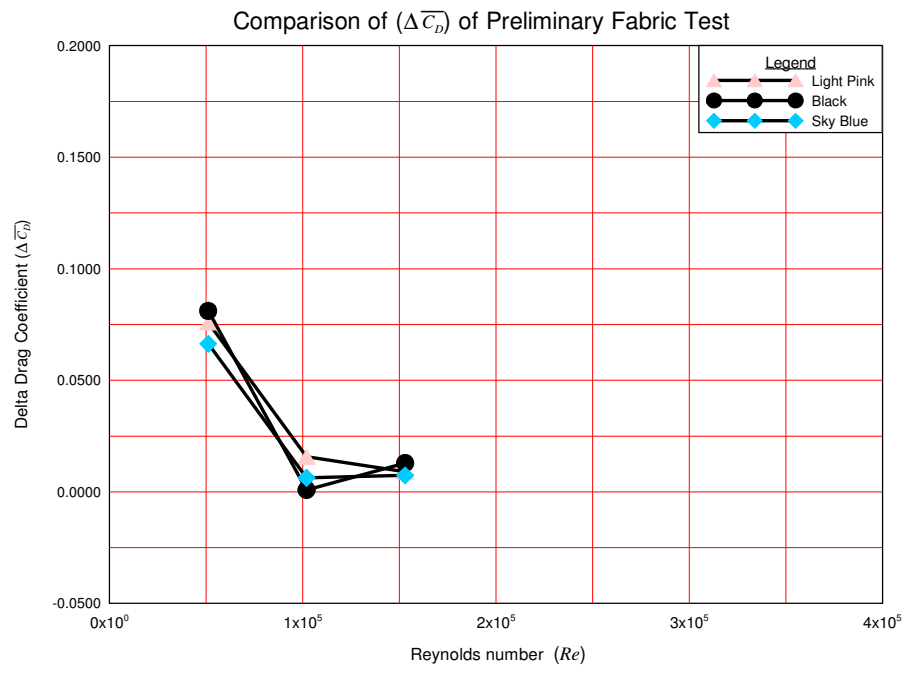


Figure 3.24c. Delta Average Drag Coefficient of Preliminary Fabric Test.

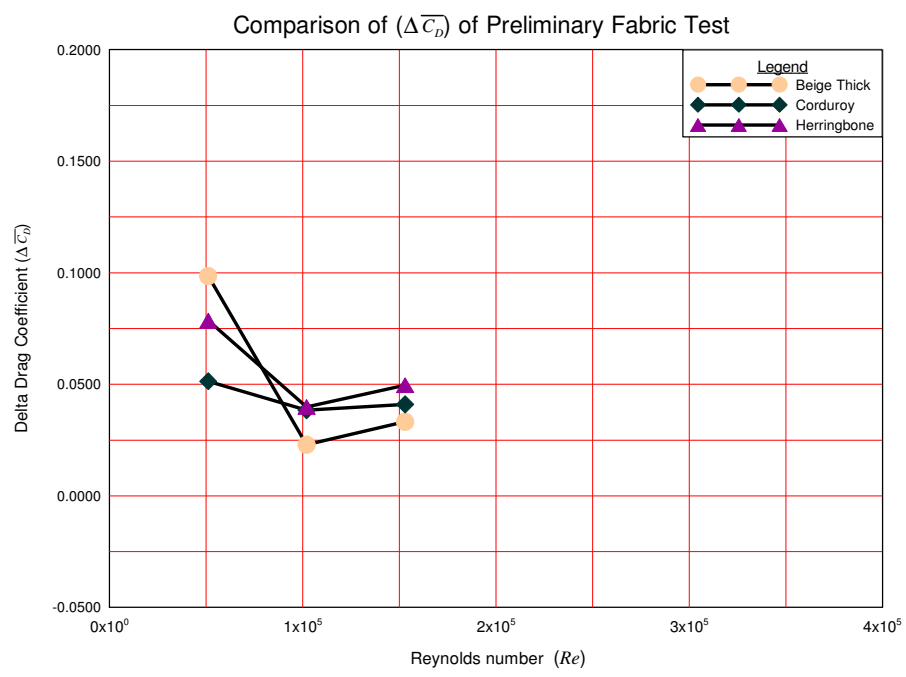


Figure 3.24d. Delta Average Drag Coefficient of Preliminary Fabric Test.



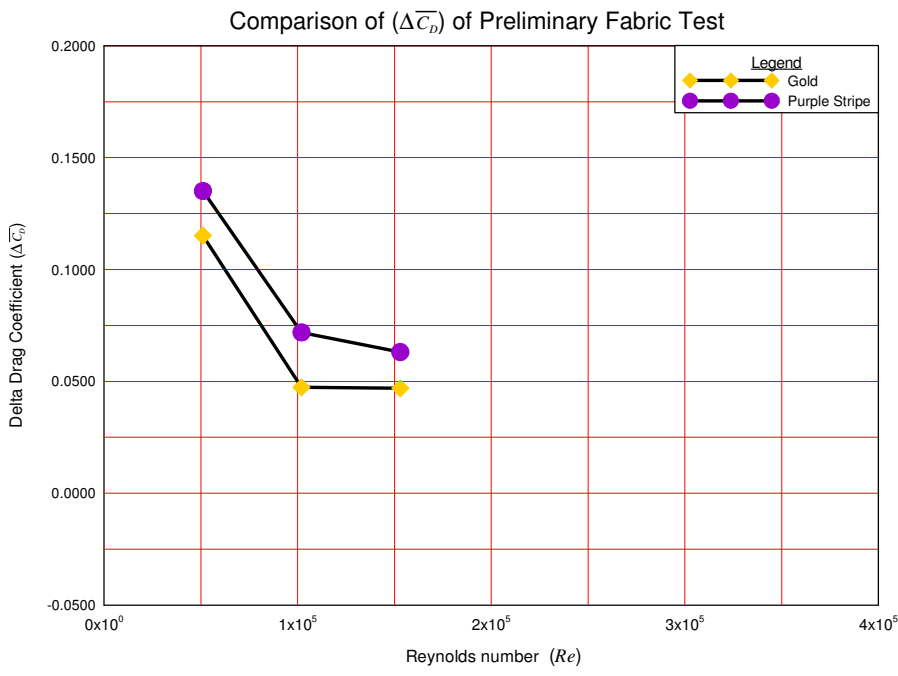


Figure 3.24e. Delta Average Drag Coefficient of Preliminary Fabric Test.

The plot of the average drag coefficient of the aluminum wing model and aluminum wing model with boundary layer trip is shown in Fig. 3.24.  $\overline{\Delta C_D}$  was calculated for the wing models with fabric skins in the final fabric test. Figure 3.25 shows the plot of delta average drag coefficient versus Reynolds number. This plot shows the net effect of the fabrics on drag reduction and will be compared to the  $\overline{C_D}$  of the aluminum wing model with the boundary layer trip.

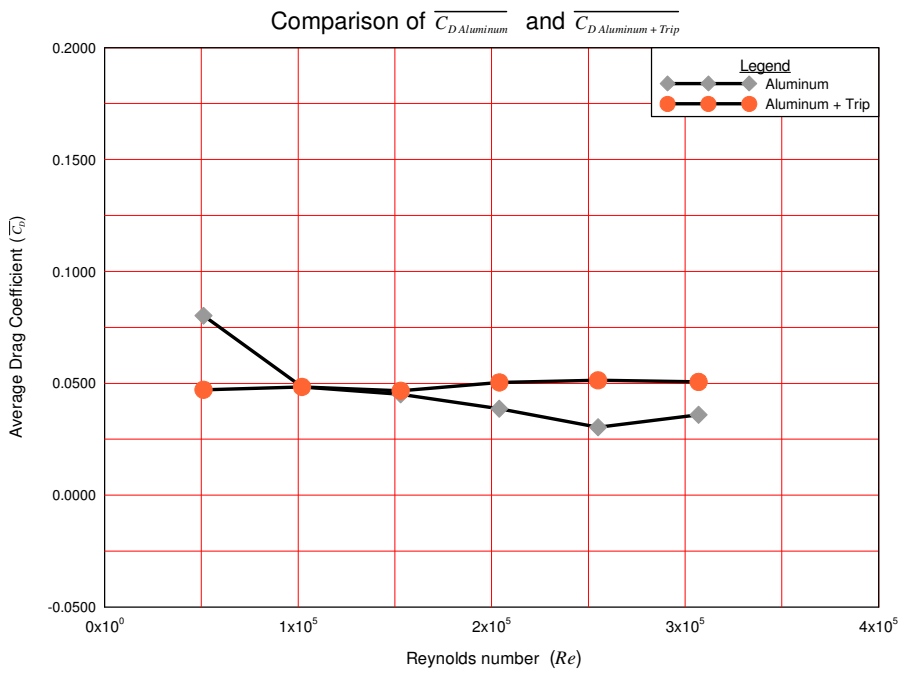


Figure 3.25. Average Drag Coefficient of Aluminum Wing Model (with/without trip).  
*The trip strip smoothed the curve.*

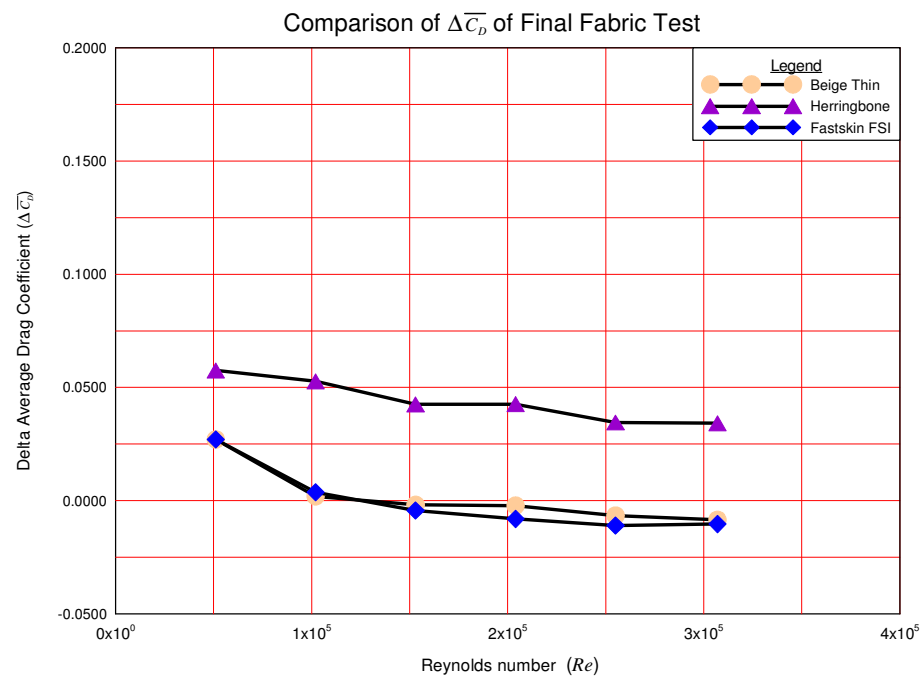


Figure 3.26. Delta Average Drag Coefficient of Final Fabric Test.

From Fig. 3.25, it can now be seen that the average drag coefficient of aluminum wing model with boundary layer trip is higher than the  $\overline{C_D}$  of the aluminum wing model, which is expected. Therefore, the boundary layer trip has been effective in producing a turbulent boundary layer over the surface of the airfoil at these low chord Reynolds numbers.

Notice from the results in Fig. 3.26 that the  $\Delta\overline{C_D}$  of the wing models with the fabric skins is relatively high at the lowest value of  $Re = 0.5 \times 10^5$ . This outcome is because the boundary layer at very low Reynolds number, separates from the surface into a thicker wake [1]. The flow becomes reversed at the separation point and the shear stress there is zero [1]. The boundary layer does not reattach at the rear of the wing model, as shown in Fig. 3.27.

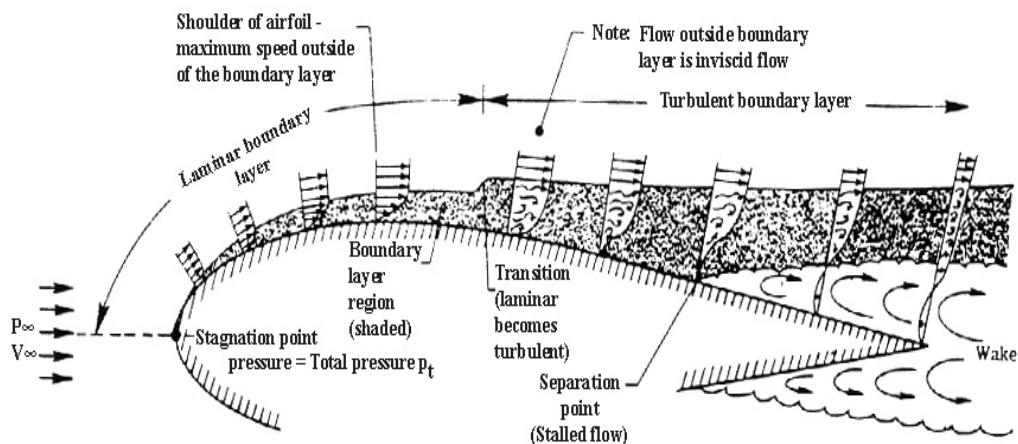


Figure 3.27. Laminar and Turbulent Boundary Layers on an Airfoil [38].

From Fig. 3.26, notice that the wing model with Fastskin<sup>®</sup> FSI and Beige Thin fabric had mostly negative values of Delta Average Drag Coefficient when compared to

the aluminum wing model with the boundary layer trip. The Fastskin<sup>®</sup> FSI and Beige Thin tends to reduce drag, and the trend seems to maintain with increasing Reynolds number.

The weave pattern of Fastskin<sup>®</sup> FSI and Beige Thin fabric has been shown in Figs. 3.3 and 3.6. In this research, the fabrics were oriented in the streamwise direction of the airflow. Notice that the Fastskin<sup>®</sup> FSI swimsuit fabric had well-defined ribs throughout the fabric and the riblets or weaves have a certain height,  $h^+$ . The ribs in the case of Beige Thin fabric were not as deep as those present in the Fastskin<sup>®</sup> FSI swimsuit fabric. The riblets were at a certain height,  $h^+$  in the case of Beige Thin fabric. The concept of protrusion height of riblets in the viscous regime has been discussed by Jimenez [39], in his review on turbulent flows over rough walls.

Define the streamwise, wall-normal and spanwise coordinates by  $x$ ,  $y$  and  $z$ ; and the corresponding velocity components be  $u$ ,  $v$  and  $w$  [39]. There is a thin near-wall region in turbulent flows over smooth walls where viscous effects are dominant. If there are small protrusions in this layer, in this case the riblet height of the fabric, the outer flow of air can be represented as having a uniform shear. If the spacing of the ribs in the fabric is small, the flow would still behave as having uniform shear, otherwise, the riblets tend to destroy this uniformity near the wall region [39]. Because the riblets are uniform in the streamwise direction, the shear stress varies very slowly in the  $x$  coordinate with respect to the dimensions of the riblets. As a consequence of this slight variation, it is likely that there is less skin friction drag and so the Fastskin<sup>®</sup> FSI swimsuit fabric and Beige Thin fabric were able to reduce the drag.

The effect of adverse pressure gradients on riblets was first reviewed by Walsh [40]. The skin friction of adverse pressure gradient boundary layers tend to be low [39]. He [40] found that the performance of the riblets improved under adverse pressure gradient conditions. From Fig. 3.26, it is seen that the  $\overline{\Delta C_D}$  of Fastskin<sup>®</sup> FSI swimsuit fabric and Beige Thin fabric were relatively low with increasing Reynolds number. The data tend to indicate that the surface patterns in the fabrics drive the separation point rearward, keeping the flow attached on the surface and maintaining a thinner wake region at the rear end of the wing model with fabric skins. The flow could be accelerated relative to the surface by the ribs, which is believed to channelize the airflow [40].

For an incompressible flow, the flow velocity is split into a mean part and a fluctuating part using Reynolds decomposition [41] which for the  $x$  component is given as

$$u = \bar{u} + u' \quad (6)$$

where,  $u$  is the flow velocity vector,  $\bar{u}$  is the mean velocity that is determined by time averaging and  $u'$  is the fluctuating part of the velocity vector [41]. The equation is similar for the  $v$  and  $w$  velocity components. Bhushan [5] and Jiminez [39] explain that the streamwise eddies are displaced away from the wall when the airflow interacts with the riblets and the turbulent mixing of streamwise momentum is reduced. This mixing leads to higher local shear stress near the wall but the reduced mixing results in lower skin friction drag [39]. The fabrics are believed to stabilize the fluctuating part of the velocity component.

From Fig. 3.26, it is seen that the Herringbone fabric could not reduce drag because the spacing of ribs and the height of the riblets were very large when compared to the Fastskin® FSI swimsuit fabric and Beige Thin fabric. In the case of Herringbone, the ribs were also not aligned. Furthermore, a large amount of “fuzzyiness” was present in this fabric and it was also porous. The porosity in fabrics decreases the airflow velocity [21].

In conclusion, fabrics with certain riblet height and spacing between the ribs appear to reduce drag. Rough surfaces can be used as a drag reduction technique. The next chapter discusses the conclusions of this research, potential applications and future work.

## Chapter 4

### Conclusions

In this research, NACA 0012 wing models with fabric skins were tested at low Reynolds numbers ( $10^4$  to  $10^5$  range) at zero incidence to assess their effectiveness in reducing drag. A similar wing model with an aircraft aluminum alloy skin and a boundary layer trip strip served as a baseline for drag comparison. The wing models with riblets aligned in the streamwise direction of airflow were tested in a small subsonic wind tunnel and drag force measurements were made. The following conclusions have been drawn from the study:

1. It was observed that the delta average drag coefficient of the Fastskin<sup>®</sup> FSI swimsuit fabric and Beige Thin fabric were lower than that of the aluminum wing model with the boundary layer trip strip and the trend was maintained with increasing Reynolds number.
2. In the case of Herringbone, the drag was substantially higher. The ribs were not aligned with the streamwise direction of airflow, a large amount of “fuzziness” was present in the fabric, and it was porous.
3. It was noticed that the fabrics with certain riblet height and spacing of ribs, similar to Fastskin<sup>®</sup> FSI exhibited the least drag.
4. From the tests performed on fabric skins, it was observed that certain ribbed surface structures can reduce drag.

#### **4.1 Future Work**

A shorter, smaller diameter sting would help reduce sting only drag and aerodynamic “fluctuations” leading to cleaner drag measurements dominated by model drag. In the future, it is suggested to adhere fabric skins to larger wing models and test them in larger wind tunnels. This would help evaluate fabric performance at higher Reynolds numbers. Flow visualization at the microscopic scale is needed to increase the understanding of riblets and their effect on reducing drag.

#### **4.2 Potential Applications and Methods**

Aerospace and other products where drag reducing fabric based riblet patterns can be incorporated are:

- As skins and covers for complex aerodynamic and hydrodynamic shapes.
- Adhered or impregnated into aerodynamic or hydrodynamic surfaces for drag reduction.



## References

1. Anderson, J.D., *Fundamentals of Aerodynamics*, 5<sup>th</sup> ed., McGraw-Hill, New York, 2010.
2. Rethorst, S. C., Pasadena, CA, U.S. Patent Application for a “Ridge Surface system for maintaining laminar flow,” U.S. Patent No. 3,588,005, patented 28 Jun. 1971.
3. Munson B., Young D., and Okushi T., *Fundamentals of Fluid Mechanics*, 5<sup>th</sup> ed., Wiley, New York, 2005.
4. Aupoix, B., Pailhas, G., and Houdeville, R., “Towards a General Strategy to Model Riblet Effects,” *AIAA Journal*, Vol. 50, No. 3, 2012, pp. 708-716.
5. Bhushan, B., *Biomimetics: Bioinspired Hierarchical-Structured Surfaces for Green Science and Technology*, Biological and Medical Physics, Biomedical Engineering, Springer, New York, 2012.
6. Choi, H., “Biomimetic Flow Control,” *62<sup>nd</sup> APS Division of Fluid Dynamics*, Minneapolis, MN, 2009.
7. Bullen, R.D., and McKenzie, N.L., “The pelage of bats (Chiroptera) and the presence of aerodynamic riblets: the effect on aerodynamic cleanliness,” *Zoology*, Vol. 111, Issue 4, 2008, pp. 279-286.
8. “Bat Hair,” *MicrolabNW Photomicrograph Gallery* [online database], URL: <http://www.microlabgallery.com/gallery/HairBatNearRoot.aspx> [cited 28 April 2015].
9. Trevor, S., “Biomimicry Shark Denticles,” URL: <http://ocean.si.edu/ocean-photos/biomimicry-shark-denticles> [cited 28 April 2015].
10. Walsh, M.J., Anders, J.B., and Hefner, J.N., Newport News, VA, U.S. Patent Application for a “Combined riblet and LEBU drag reduction system,” U.S. Patent No. 4,706,910, patented 17 Nov. 1987.
11. Walsh, M.J., and Weinstein, L.M., “Drag and Heat Transfer on Surfaces with Longitudinal Fins,” *AIAA Journal*, Vol. 17, No. 7, 1978, pp. 78-1161.
12. Liu, C.K., Kline, S.J, and Johnston, J.P., “An Experimental Study of Turbulent Boundary Layers on Rough Walls”, Thermosciences Div., Mechanical Engineering Dept., Stanford Univ., Stanford, CA, Rept. MD-15, 1966.
13. Bechert, D.W., and Bartenwerfer, M., “The Viscous Flow on Surfaces with Longitudinal Ribs,” *Journal of Fluid Mechanics*, Vol. 206, 1989, pp 105-129.

14. Choi, K.S., "Effect of Longitudinal Pressure Gradient on Turbulent Drag Reduction with Riblets," *Turbulence Control by Passive Means*, edited by E. Coustols, Kluwer Academic, Norwell, MA, 1992, pp. 109-120.
15. Sundaram, S., Viswanath, P.R., and Rudrakumar, S., "Viscous Drag Reduction Using Riblets on NACA 0012 Airfoil to Moderate Incidence," *AIAA Journal*, Vol. 34, No. 4, 1996, pp. 676-682.
16. "Micrographs of Experimental 3M Riblet Film," URL: <http://www.safl.umn.edu/featured-story/featured-research-project-reducing-wind-turbine-blade-drag-using-riblet-film> [cited 23 February 2015].
17. "The Speedo Story," URL: <http://www.insidespeedo.com/our-heritage> [cited 23 February 2015].
18. "Swim like a shark!," URL: <http://www.scienceinthenews.org.uk/contents/?article=8> [cited 20 February 2015].
19. Coustols, E., and Cousteix, J., "Experimental Investigation of Turbulent Boundary Layers Manipulated with Internal Devices: Riblets," *Structure of Turbulence and Drag Reduction*, Springer-Verlag, New York, 1990, pp. 577-584.
20. Coustols, E., "Riblets: Main Known and Unknown Features," *Emerging Techniques in Drag Reduction*, edited by K S Choi, K K Prasad, T V Truong, *Mechanical Engineering Publications*, 1996, pp. 3-44.
21. Watanabe, T., Kato, T., and Kamata, Y., "The Velocity Distribution in the Inner Flow Field around a Clothed Cylinder," *Sen'i Gakkaishi*, Vol. 47, No. 6, 1991.
22. "Plastics Technical and Installation Manual," *Charlotte Pipe and Foundry Company* [online database], URL: [http://www.charlottepipe.com/Documents/PL\\_Tech\\_Man/Charlotte\\_Plastics\\_Tech\\_Manual.pdf](http://www.charlottepipe.com/Documents/PL_Tech_Man/Charlotte_Plastics_Tech_Manual.pdf) [cited 3 March 2015].
23. "Corrosion-Resistant 304 Stainless Steel Woven Wire Cloth," *McMaster-Carr* [online database], URL: <http://www.mcmaster.com/#85385t49/=waienu> [cited 5 March 2015].
24. Arifuzzaman, Md., and Mashud, M., "Design Construction and Performance Test of a Low Cost Subsonic Wind Tunnel," *IOSR Journal of Engineering*, Vol. 2, Issue 10, 2012, pp. 83-92.
25. "Corrosion-Resistant 304 Stainless Steel Woven Wire Cloth," *McMaster-Carr* [online database], URL: <http://www.mcmaster.com/#85385t62/=waih52> [cited 5 March 2015].

26. Lee, B., "Aluminum Honeycomb, Aluminum Composite Panel," URL: [http://www.seoultrademall.com/co/bruceleesorne/Aluminum\\_Honeycomb\\_Aluminum\\_Composite\\_Panel...-1476149\\_1476199.html](http://www.seoultrademall.com/co/bruceleesorne/Aluminum_Honeycomb_Aluminum_Composite_Panel...-1476149_1476199.html) [cited 3 March 2015].
27. "Impact-Resistant Polycarbonate Round Tube," *McMaster-Carr* [online database], URL: <http://www.mcmaster.com/#8585k74/=wajiv5> [cited 5 March 2015].
28. "PVC Gate Valve," *McMaster-Carr* [online database], URL: <http://www.mcmaster.com/#9762K15/=Wy7011> [cited 5 March 2015].
29. "Owner's Manual (General)," *Shop-Vac Corporation* [online database], URL: <http://www.appliancefactoryparts.com/vacuumcleaners/brands/shop-vac/1l600.html> [cited 5 March 2015].
30. "Series Load Cells Catalog Number 2530-400," *Instron* [online database], URL: <http://www.instron.com/~media/literature-library/products/2003/08/2530-400-series-load-cells.pdf?la=en> [cited 5 March 2015].
31. "Sorbothane Overview," *Sorbothane, Incorporated* [online database], URL: <http://www.sorbothane.com/> [cited 5 March 2015].
32. "Ultra-Soft Polyurethane Sheet," *McMaster-Carr* [online database], URL: <http://www.mcmaster.com/#8514k53/=wy9p0z> [cited 5 March 2015].
33. "Anodized Aluminum Round," *The Hillman Group* [online database], URL: <http://wedo.hillmangroup.com/item/metal-shapes/anodized-aluminum-round/item-12766> [cited 5 March 2015].
34. "Pitot-Static," *United Sensor Corporation* [online database], URL: <http://www.unitedsensorcorp.com/pitot-pa.html> [cited 28 April 2015].
35. Hoerner, S.F., *Fluid-Dynamic Drag*, 2<sup>nd</sup> ed., Hoerner Fluid Dynamics, Bricktown, NJ, June 1965.
36. "Drag of Cylinders & Cones," URL: <http://www.aerospaceweb.org/question/aerodynamics/q0231.shtml> [cited 28 April 2015].
37. Rona, A. and Soueid, H., "Boundary Layer Trips for Low Reynolds Number Wind Tunnel Tests," *AIAA Aerospace Sciences Meeting Including the New Horizons Forum and Aerospace Exposition*, AIAA, Orlando, FL, 2010.
38. "High-Lift Devices," URL: <http://aerospaceengineeringblog.com/high-lift-devices/> [cited 12 February 2015].

39. Jimenez, J., and Mayoral, R.G., "Drag reduction by riblets," *Philosophical Transactions of the Royal Society A*, 369, 2011, pp. 1412-1427.
40. Walsh, M.J., "Riblets," *AIAA Journal*, 1990, pp. 203-26.
41. "Turbulent Flow - Reynolds Stresses," URL: <http://ocw.mit.edu/courses/mechanical-engineering/2-20-marine-hydrodynamics-13-021-spring-2005/lecture-notes/lecture18.pdf> [cited 19 May 2015].

## Appendix A

### Bibliography

“Some Basics on Drag,” URL: [http://cyclingdynamics.blogspot.com/2013\\_10\\_01\\_archive.html](http://cyclingdynamics.blogspot.com/2013_10_01_archive.html) [cited 23 February 2015].

“Flow Past a Cylinder,”

URL: <http://www.grc.nasa.gov/WWW/k-12/airplane/dragSphere.html> [cited 27 February 2015].

Baals, D.D., and Corliss, W.R., “Wind tunnels of NASA, Whirling Arms and the First Wind Tunnels,” URL: [www.grc.nasa.gov/WWW/k12/WindTunnel/history.html](http://www.grc.nasa.gov/WWW/k12/WindTunnel/history.html) [cited 3 March 2015].

“Wind Tunnel,” URL: [http://en.wikipedia.org/wiki/Wind\\_tunnel](http://en.wikipedia.org/wiki/Wind_tunnel) [cited 3 March 2015].

Tom, B., “Types of Wind Tunnels,” URL: <http://www.grc.nasa.gov/WWW/K-12/airplane/tuntype.html> [cited 3 March 2015].

Barlow, J.B., Rae, W.H., and Pope, A., *Low Speed Wind Tunnel Testing*, 3<sup>rd</sup> ed., Wiley-Interscience, Hoboken, NJ, 1999.

Prandtl, L., “Attaining a Steady Air Stream in Wind Tunnels,” *National Advisory Committee for Aeronautics*, Vol. 4, Part 2, 1933, pp. 65-106.

Bradshaw, P., and Pankhurst, R.C., “The Design of Low-Speed Wind Tunnels,” *Progress in Aeronautical Sciences*, Vol. 5, 1964, pp. 1-69.

Tropea C., Yarin, A.L, and Foss, J.F., *Springer Handbook of Experimental Fluid Mechanics*, Springer-Verlag, New York, 2007.

“Flow through Pipes,”

URL: <http://www.engineershandbook.net/wp-content/uploads/2013/08/Pipe-flow.jpg> [cited 23 February 2015].

“Hot-Wire Anemometers: Introduction,”

URL: [http://www.efunda.com/designstandards/sensors/hot\\_wires/hot\\_wires\\_intro.cfm](http://www.efunda.com/designstandards/sensors/hot_wires/hot_wires_intro.cfm) [cited 28 April 2015].

“Differential Manometer,” URL: <http://encyclopedia2thefreedictionary.com/Differential+Manometer> [cited 28 April 2015].

**Appendix B**  
**Additional Figures and Tables**



Figure B1. Test Models.  
*Sphere, Cube, Wooden Bird, and F-16 Model (left to right).*



Figure B2. Wooden Bird with Chart Paper Background.  
*The reference area was conveniently found in this way. The smallest squares are 1 mm<sup>2</sup>*

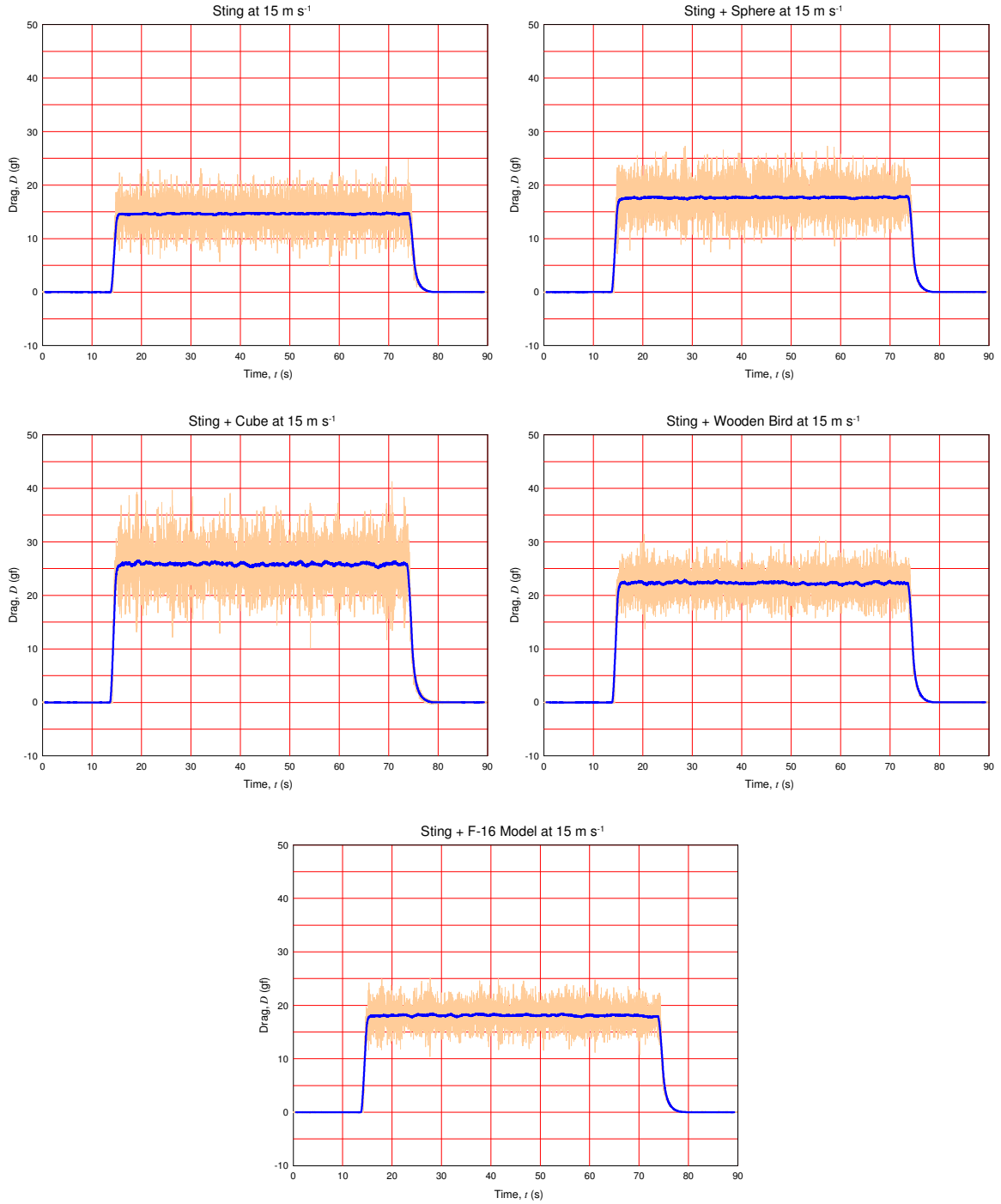


Figure B3. Test Models at  $15 \text{ m s}^{-1}$ .

*The actual data with aerodynamic fluctuations is shown in tan while the 101 point moving average is shown in blue. The F-16 model shows the least fluctuations. Similar trends for the differing models were seen at all velocities.*

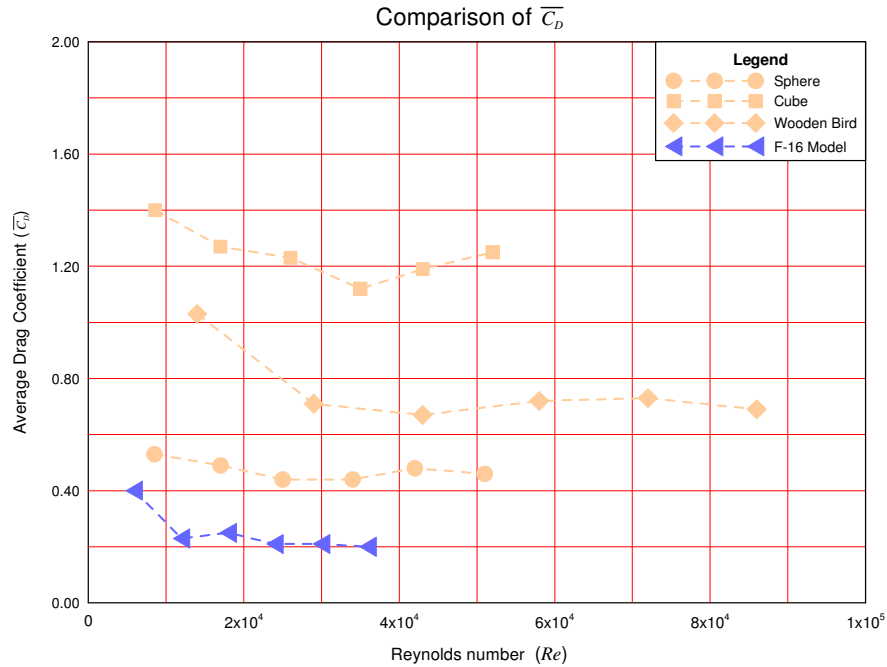


Figure B4. Average Drag Coefficient of Test Models.  
 Dimension used for Reynolds number: Sphere (diameter), Cube (side), Wooden Bird (height), F-16 Model (mean chord).

Table B1. Test Model Details.

Test Model	Specification	Manufacturer/Supplier	Measured Dimension(s) (cm)	$S$ (cm <sup>2</sup> )
Sphere	Wood, Round Ball Knob, 1 in	The Hillman Group (Cincinnati, OH)	2.54 (diameter)	5.07
Cube	Wood, Square Cube, 1 in	The Hillman Group (Cincinnati, OH)	2.57 (side)	6.60
Wooden Bird	ArtMinds™ Wooden Bird	Michaels Stores, Inc. (Irving, TX)	4.30 (height)	8.25
F-16	In Air® F-16 Fighting Falcon®, diecast	WowToyz (Vergennes, VT)	$b/2 = 2.83$ , $c_r = 2.87$ , $c_l = 0.66$	9.99 (wing area)



Table B2. Product and Equipment Information.

Product/Equipment	Specification	Manufacturer/Supplier
Data Acquisition	8802 Test System with FastTrack 8800 Controller and DAX V9.1	Instron (Norwood, MA)
Calibration Weights	Class S-1 and 100 g Class F precision calibration weights	Troemner (Thorofare, NJ)
Sandpaper	320 and 600 grit SiC	Leco Corp. (St. Joseph, MI)
Calipers	Pittsburgh® 6 in Digital Caliper	Harbor Freight Tools (Camarillo, CA)
Digital Camera	EOS Rebel T1i with EF-S 18-135 f/3.5-5.6 IS STM lens	Canon U.S.A., Inc. (Melville, NY)
Thermocouple	Type K with 52 II Thermometer	Fluke Corp. (Everett, WA)
Pressure Calibrator	PCL341-005 Pressure Calibrator	Omega Engineering Inc. (Stamford, CT)
Wing Cores	EPS (expanded polystyrene), NACA 0012, 6 in chord, round leading edge	FlyingFoam (Fort Collins, CO)
Sectioning Machine	MSX255 Benchtop Sectioning Machine	Leco Corp. (St. Joseph, MI)
Sting Mount	Round C260 brass tube with 9/32 in OD and 0.253 in ID	Small Parts Inc. (operated by amazon.com, Seattle, WA)
Forming Blocks	6061-T6511 Al alloy, 1 in square	McMaster-Carr Supply Co. (Elmhurst, IL)
Screw Driven Test Machine	Model 290 Lo-Cap Universal Testing Machine	Tinius Olsen Testing Machine Company (Horsham, PA)
Foam Fill	Touch 'n Foam Max Fill	Convenience Products (Fenton, MO)
Swimsuit	Fastskin® FSI	Speedo International Ltd. (Nottingham, UK)
Fabric Adhesive	Polystyrene Foam Insulation 78 Spray Adhesive	3M Company (Saint Paul, MN)
Al Skin	2024-T3, 0.012 in	Kaiser Aluminum (Foothill Ranch, CA)
Al Skin Adhesive	SilverTip MetlWeld™ Epoxy Adhesive	System Three Resins, Inc. (Auburn, WA)
Trip Strip Adhesive	Gorilla Epoxy	Gorilla Glue Inc. (Cincinnati, OH)
Microscope	Stereomaster® II	Thermo Fisher Scientific (Pittsburgh, PA)
Microscope Camera	PLB623CU, 3 megapixel, Capture OEM Release 8.7 software	PixeLINK® (Ottawa, Ontario, Canada)
Chart Paper	9270-1024 HP Chart Paper	Imaging Products (Chesterland, OH)

Table B3. Fabric Details.

Fabric	Identifier(s)	Comment
Navy Blue	DA 1005;100;163	Velvet on one side; feels like polyester
Fastskin <sup>®</sup> FSI	Barcode: 38950 69359; 705848; 043; B10788; LL	Grooves possibly added later on by some type of pressing or rolling process; LYCRA <sup>®</sup> ; ML HI neck kneeskin; royal blue
Purple	Barcode: HAC1000413 24475 8819 103	Crimped; transparent; feels like polyester
Pattern	-	Dyed; feels like polyester
Beige Thin	Barcode: HAB0842329 7051 84278 101; Separate Barcode: 5109; FC	Manufactured by Sunrise Madanlal <sup>®</sup> Suiting; ribbed on one side; feels like polyester
Diamond	Barcode: HAA 0220753 28139 85656 656; \$HL DY + Towel DGN PE 3016	Marketed by The Chennai Silks, India; looks like artificial silk
Sky Blue	08745; 90	Dyed; feels like polyester
Black	Barcode: HBC3259812 22636 84269 16684; Separate Barcode: 5109; 36639; MCM 13	Manufactured by HARROLT; marketed by The Chennai Silks, India; made from filament and spun yarn
Light Pink	Barcode: GJD1375355 13080 8807 100; DIANA 223888; MCM 40	Marketed by The Chennai Silks, India; feels like polyester
Corduroy	Barcode: GJA9980657 19404 84291; Separate Barcode: 5109; FC	Ribbed on one side; feels like cotton
Beige Thick	-	Ribbed on one side; feels like cotton and polyester
Herringbone	DA3567; 4132/TF-HL TOWE/PYRAM/162*; 06; MIA	100% cotton
Gold	BA3121; 90	Velvet on one side; feels like polyester
Purple Stripe	CA8004; 01268/TF-Towel/1/GOL/NS; 05; UI	Feels like cotton

*All fabrics except Fastskin<sup>®</sup> FSI were obtained from local textile shops in India (Trichy, Tamil Nadu) during summer 2014.*